

The dark matter haloes of Chandra X-ray galaxy clusters and baryons effect

Iu. Babyk^{1,4,5,6*}, I. Vavilova^{4†}, A. Del Popolo^{2,3‡}

¹Faculty of Physics of National Taras Shevchenko University of Kyiv, Glushkova ave., 2, 03127, Kyiv, Ukraine

²Dipartimento di Fisica e Astronomia, Università di Catania, Viale Andrea Doria 6, 95125 Catania, Italy

³Departamento de Astronomia, Universidade de São Paulo, Rua do Matão 1226, 05508-900, São Paulo, SP, Brazil

⁴Main Astronomical Observatory NAS of Ukraine, Zabolotnogo str., 27, 03650, Kyiv, Ukraine

⁵Dublin Institute for Advanced Studies, 31 Fitzwilliam Place, Dublin 2, Ireland

⁶Dublin City University, Dublin 9, Ireland

Accepted _____ . Received _____ ; in original form _____

ABSTRACT

We present results based on Chandra observations of a large sample of 129 hot galaxy clusters. We measure the concentration parameter c_{200} , the dark mass M_{200} and the baryonic mass content in all the objects of our sample, providing the largest dataset of mass parameters for galaxy clusters in the redshift range $z = 0.01 - 1.4$. We confirm that a tight correlation between c_{200} and M_{200} , $c \propto M_{vir}^a / (1+z)^b$ with $a = -0.56 \pm 0.15$ and $b = 0.80 \pm 0.25$ (68 per cent confidence limits), is present, in good agreement with the predictions from numerical simulations and previous observations. Fitting the mass profile with a generalized NFW model, we got the inner slope α , with $\alpha = 0.94 \pm 0.13$. Finally, we show that the inner slope of the density profile, α correlates with the baryonic mass content, M_b : namely α is decreasing with increasing baryonic mass content.

Key words: cosmology–theory–large scale structure of Universe–galaxies–formation

1 INTRODUCTION

The problem of dark matter halos formation has a long history going back to the seminal paper of Gunn & Gott (1972) and Gunn (1977), who studied the density profile formation using the collapse of a spherical perturbation in an expanding background. The quoted papers and several following analytical models (e.g., Fillmore & Goldreich 1984; Bertschinger 1985; Hoffman & Shaham 1985), found that density profiles are described by power-laws in all the radius range. More recent semi-analytical models (e.g., White & Zaritsky 1992, Subramanian et al. 2000; Del Popolo et al. 2000; El-Zant et al. 2001, El-Zant et al. 2004; Hiotelis 2002; Le Delliou & Henriksen 2003; Ascasibar et al. 2004; Williams et al. 2004; Tonini et al. 2006; Ascasibar et al. 2007) showed that the profile is not a power-law, similarly to N-body simulations results (e.g., Navarro et al. (1996), Navarro et al. (1997)); Navarro–Frenk–White (NFW)), Moore et al. 1998; Jing & Suto 2000; Klypin et al. 2001,

Bullock et al. 2001, Power et al. 2003, and Navarro et al. 2004, Navarro et al. 2010) found that the spherically averaged density profiles of the N-body DM halos are similar, regardless of the mass of the halo or the cosmological model. The NFW profile is given by:

$$\rho(r) = \frac{\rho_0}{r/r_s(1+r/r_s)^2} = \frac{\rho_{critic}\Delta_c}{r/r_s(1+r/r_s)^2} \quad (1)$$

where ρ_{critic} is the critical density of the Universe at the cluster’s redshift z , and Δ_c is the virial overdensity. The scale radius r_s is connected to the virial radius r_{vir} through the concentration parameter c , $c = r_{vir}/r_s$. At small scales, the logarithmic density slope, that is also known as inner slope, is given by

$$\alpha = -\left.\frac{d \log \rho}{d \log r}\right|_{r \rightarrow 0} = 1 \quad (2)$$

The quoted profile diverges as $\rho \propto r^{-1}$ in the inner part, and at large radii behaves as $\rho \propto r^{-3}$. The inner

¹ Since r_{vir} is difficult to determine observationally, its value is often approximated by the radius within which the average density is greater than the critical density by a specified factor (e.g., 200). In the following of the paper, r_{vir} is identified with r_{200} .

* E-mail: babikyura@gmail.com

† E-mail: iriv@mao.kiev.ua

‡ E-mail: antonino.delpopolo@unibg.it

slope is even steeper in Moore et al. (1998) profile ($\rho \propto r^{-1.5}$). More recent simulations (e.g., Power et al. 2003, Hayashi et al. 2004, and Navarro et al. 2004, Navarro et al. 2010; Stadel et al. 2009) showed that density profiles are better fitted by the Einasto profile, which becomes shallower towards the centre of the halo.

Unfortunately, N-body simulations predictions are not supported by observations. Observations of the inner part of density profiles of dwarf galaxies and LSBs are characterized by a core-like structure (e.g. Flores & Primack 1994; Moore 1994; de Blok & Bosma 2002; de Blok et al. 2003; Gentile et al. 2004, Salucci et al. 2007; Kuzio de Naray et al. 2008, Kuzio de Naray et al. 2009), and a similar problem is evidenced when studying the clusters of galaxies inner profile. Density profiles of clusters has been studied through X-ray observations, strong and weak lensing. X-ray temperature measurements give information on cluster structure in the range 500-50 kpc (Bradač et al. 2008). At smaller radii, temperature determination is limited by instrumental resolution or substructure (Schmidt & Allen 2007, hereafter SA07). X-ray measurements are also limited by “cooling flows” presence, and the breaking of assumption of hydrostatic equilibrium (see Arabadjis et al. 2004). The inner slope calculation through the use of X-ray observations brought to discrepant values (e.g., 0.6 (Ettori et al. 2002), 1.2 (Lewis et al. 2003), 1.9 (Arabadjis et al. 2002).

Another technique used to study the DM distribution in clusters is gravitational lensing. Weak lensing of background galaxies is used to reconstruct the mass distribution in the outer parts of clusters (Mellier 1999). The resolution that can be achieved is able to constrain profiles inside 100 kpc. Strong lensing is used to study the DM distribution in the inner parts of clusters, it has a typical sensitivity to the projected mass distribution inside $\simeq 100 - 200$ kpc, with limits at $\simeq 10 - 20$ kpc (Gavazzi 2005; Limousin et al. 2008, Alexandrov et al. 2011; Tsvetkova et al. 2009).

Discrepant results have been sometime obtained when using the lensing method. Smith et al. (2001), found $\alpha > 1$ at 1% of r_{vir} by studying the tangential and radial arcs of A383. A much smaller value α was obtained by Sand et al. (2004) and Newman et al. (2011), for the same cluster, using lensing and through the aid of stellar kinematics of the central region. Tyson et al. (1998) found $\alpha = 0.57 \pm 0.024$ for Cl 0024+1654, while Kneib et al. (2003) found that a NFW profile fits the profile in the radius range 0.1-several r_{vir} . Sand et al. (2002) found a cored profile with $\alpha = 0.35$ for MS2137.3-2353, while Gavazzi et al. (2003) and Gavazzi (2005) concluded that the precise value of the slope depends on the mass-to-light ratio of the Brightest Cluster Galaxy (BCG).

In summary, N-body simulations are not always in agreement with the inner slopes of dwarf galaxies, LSBs and clusters of galaxies, and in the case of clusters of galaxies, observations may even disagree for the very same cluster (Gavazzi 2005 ; Smith et al. 2005; Zappacosta et al. 2006; SA07; Bradač et al. 2008; Limousin et al. 2008; Umetsu & Broadhurst 2008).

Several could be the reasons of the discrepancy (e.g., (a) different definition of the slope, which sometimes refers to the DM and sometimes to the total mass; (b) use of observational techniques with different/limited dynamic range

in radius; (c) not taking into account the stellar mass of the BCG). In order to obtain more sure constraints on the central part of the density profiles, one should use combined methods (Miralda-Escude 1995; Kneib et al. 2003 (weak+strong lensing); Bradač et al. 2005 (weak+strong lensing); Mahdavi et al. 2007 (X-ray+weak lensing)), or better constraints on the central part of the density profiles can be obtained through stellar kinematics of the central galaxy ($\simeq 1 - 200$ kpc region).

In a series of papers, Sand et al. (2002), Sand et al. (2004), Sand et al. (2008), studied the clusters MS 2137-23; A383; A963; RXJ1133; MACS 1206; A1201, separating the contribution to the halo coming from the DM from that coming from the baryonic and stellar mass of the BCG. They found a profile flatter than $\alpha < 1$ except for RXJ1133. Newman et al. (2011) found $\alpha < 1$ (95 per cent CL) for A383. Newman et al. (2009) presented a detailed analysis of DM and baryonic distributions in A611, finding a slope $\alpha < 0.3$ (68 per cent CL).

Summarizing, at least some clusters of galaxies have inner density-profile slopes shallower than those obtained in N-body simulations, in agreement with what happens, as previously reported, with the density profiles of dwarf galaxies and LSBs (e.g. Flores & Primack 1994; Moore 1994; de Blok & Bosma 2002; de Blok et al. 2003; Gentile et al. 2004, Salucci et al. 2007; Kuzio de Naray et al. 2008, Kuzio de Naray et al. 2009). We want to recall here that, similarly to Sand’s result concerning the quoted clusters, the galaxies NGC 2976, NGC 4605, NGC 5949, NGC5963 and NGC 6689, have inner slopes going from very flat to cuspy, and de Blok et al. (2008), using a sample from The HI Nearby Galaxy Survey (THINGS) found that the best fit to rotation curves, and then the inner slope α of their density profile, depends on their mass.

Several papers have shown the fundamental role of baryons in shaping the density profiles of structures. Different processes have been pointed out capable of flattening the inner density profile, transferring energy from stellar baryons to the dark matter, heating it and lowering the central dark matter density (Milosavljević & Merritt 2001; El-Zant et al. 2001, El-Zant et al. 2001; Weinberg & Katz 2002; Loeb & Peebles 2003; Gao & White 2007; Ma et al. 2009; McMillan & Dehnen 2005; Tonini et al. 2006; Mashchenko et al. 2006; Romano-Díaz et al. 2008, Romano-Díaz et al. 2009; Del Popolo 2009; Governato et al. 2010; Kulinich et al. 2012).

In the present paper, we use Chandra X-ray data to study, similarly to SA07, the properties of 129 dynamically relaxed galaxy clusters. We selected the sample with redshift range from 0.01 to 1.4. with the aim to recover their total and gas mass profiles and analysis of the measured distribution of c_{200} , M_{200} and baryonic mass content. We determine the baryons content of each cluster subtracting the DM from the total mass. Even if the results concerning the density profile of clusters are similar to those of SA07, we point out that fitting the density profile with a generalized NFW model

$$\rho(r) = \frac{\rho_0}{(r/r_s)^\alpha (1 + r/r_s)^{3-\alpha}} \quad (3)$$

the slope α is correlated with the baryonic mass content of the cluster, in agreement with several studies

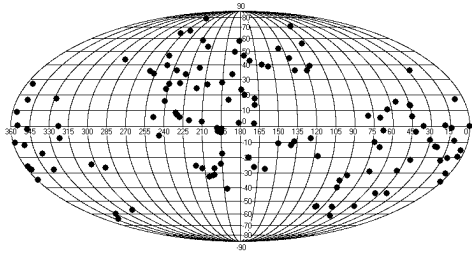


Figure 1. The distribution of galaxy clusters at the celestial sphere.

(Ricotti 2003; Subramanian et al. 2000; Simon et al. 2005; Cen et al. 2004; Ricotti & Wilkinson 2004; Williams et al. 2004; Ricotti et al. 2007; Del Popolo 2009, Del Popolo 2012). In the paper the assumed value of Hubble constant is $H_0 = 73 \text{ km s}^{-1} \text{ Mpc}^{-1}$ and $\Omega_m = 0.27$. The outline of our work is the following. In Section 2, we describe the X-ray galaxy clusters sample of Chandra observations compiled by us to recover the baryonic and total mass profiles with techniques presented in Section 3. In Section 4, we present a preliminary discussion of the main results. We investigate the $c_{200} - M_{200}$ and $\alpha - M_b$ relations. We summarize our results and draw the conclusion of the present study in Section 5 and 6.

2 SAMPLE AND DATA PROCESSING

The sample has been built to cover a wide range in redshift from 0.01 to 1.4, constituted by 129 galaxy clusters. All clusters in the sample have a regular X-ray morphology, indicative of a relaxed state and allowing reliable determination of the total mass profile through the hydrostatic equilibrium equation. The observations results are presented in Tab. 1. The preliminary processing of the Chandra data, which were obtained using the Advanced CCD Imaging Spectrometer (ACIS), included: the Chandra pipeline processing of the list of events; the re-processing with the CIAO software package; improving the rejection of cosmic ray events by VFAINT mode; cleaning the data in format of recommendation by the Chandra X-ray Centre (to remove periods of anomalously high background).

The Tab. 1 consists of the name of clusters, the redshift, the number of observation, the exposition time (before cleaning), instrument, and the values of column density, which were described by Dickey & Lockman (1990), and coordinates (RA, DEC) (which were taken from NED²). It is important to note that our list of clusters includes a few clusters with merger's properties, for example, Abell 2744, but in such case we have used only one component on the image for data reduction.

As we see in Fig.2, the most of clusters has the redshift in the range 0.01 – 0.3. We added to our sample MACS and RCSJ clusters as ones of the most distant objects which are observed by Chandra. The distribution of the studied galaxy

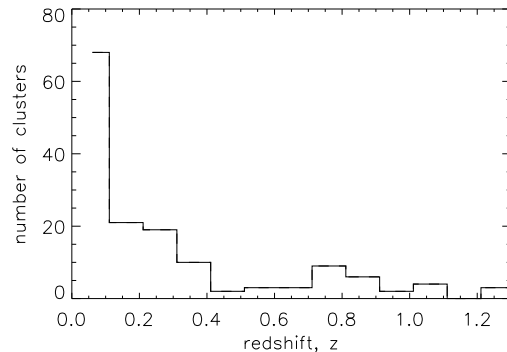


Figure 2. The distribution of galaxy clusters in our sample.

clusters at the celestial sphere is given in Fig. 1. We used in our research the sample of the clusters used by Allen et al. (2002) to study the evolution of the X-ray gas mass fraction and constrain cosmological parameters. To minimize systematic scatter and to allow the most precise test of the CDM model predictions, we used only highly relaxed clusters.

The data reduction was performed with the Chandra CIAO v.4.2 including CalDB 4.5.1 for maps and calibration. The main data processing steps were provided using techniques discussed by Babyk (2012), Babyk & Vavilova (2012), Babyk et al. (2012), Babyk et al. (2012) in our previous research. The quoted steps are the following: a) removing the point sources; b) determining the X-ray peaks; c) centering the X-ray peaks with different width to provide the same number of X-ray photons in each annulus; d) extracting the annular spectra. The average of the outermost radius is about 1 Mpc. We have generated ARF and RMF files using the mkarf and mkrmf command in CIAO tool.

We used Xspec (version 12.6)(Arnaud 1996) to analyze spectra, the MEKAL³ code (Kaastra & Mewe 1993) and WABS⁴ for fitting the data and Fe-L calculations (Liedahl et al. 1995). The content of heavy elements in this model was taken close to the solar level ($Z=0.3$) and was frozen. The energy range 0.5-7.0 keV was used during fitting, and the spectra were grouped to have at least 50 counts per spectral bin.

Background spectra were extracted from the blank-field data sets which is available from the Chandra X-ray centre, and this technique was used only for nearer galaxy clusters ($0 < z < 0.3$). For more distant clusters, the background spectra were extracted from the region which has the same size like in region for source. Usually, we used observations which were made on ACIS chips 0,1,2,3 and 7, because these chips are most accurate in calibration, although ACIS 4,5 and 6 were also used. All background spectra were cleaned as done with the main previous spectra.

We have used DSDEPROJ routine method (Sanders & Fabian 2007, Russell et al. 2008) to process the annular spectra in order to determine X-ray temperature and other parameters. After determining the temperature of clusters we built the surface brightness profile for each

² <http://nedwww.ipac.caltech.edu>

³ MEKAL is the model which describes an emission from hot diffuse plasma (ICM)

⁴ The WABS is a parameter which describe the galactic absorption (Dickey & Lockman 1990)

Table 1. Summary of the Chandra observations. Column list the target name, redshift, number of ID observation, net exposure time, detector used, column density and coordinates (taken from NED) from the X-ray centres used in the analysis.

Cluster	z	<i>ObsID</i>	t_{exp} , ks	Instrument	n_H , 10^{20} cm^{-2}	RA(J2000)	DEC(J2000)
A85	0.055	904	38.91	ACIS-I	3.26	00 41 37.8	-09 20 33
A119	0.044	7918	45.63	ACIS-I	3.44	00 56 21.4	-01 15 47
A133	0.056	2203	35.91	ACIS-S	1.55	01 02 39.0	-21 57 15
A168	0.045	3203	41.12	ACIS-I	3.48	01 15 09.8	+00 14 51
A209	0.206	522	10.09	ACIS-I	1.71	01 31 53.0	-13 36 42
A262	0.016	2215	29.12	ACIS-S	5.36	01 52 50.4	+36 08 46
A383	0.187	524	10.09	ACIS-I	3.84	02 48 06.9	-03 29 32
A399	0.072	3230	49.28	ACIS-I	11.50	02 57 56.4	+13 00 59
A401	0.074	518	18.24	ACIS-I	10.30	02 58 56.9	+13 34 56
A478	0.088	1669	42.94	ACIS-S	14.80	04 13 20.7	+10 28 35
A496	0.033	931	19.16	ACIS-S	4.45	04 33 37.1	-13 14 46
A521	0.250	430	39.60	ACIS-S	6.05	04 54 10.1	-10 15 11
A539	0.028	5808	24.60	ACIS-I	12.90	05 16 35.1	+06 27 14
A576	0.039	3289	39.10	ACIS-S	5.66	07 21 24.1	+55 44 20
A644	0.070	2211	30.08	ACIS-I	6.44	08 17 26.4	-07 35 21
A697	0.280	4217	19.70	ACIS-I	3.41	08 42 53.3	+36 20 12
A754	0.054	577	44.77	ACIS-I	4.45	09 08 50.1	-09 38 12
A773	0.217	533	10.50	ACIS-I	1.44	09 17 59.4	+51 42 23
A780	0.054	575	24.10	ACIS-I	4.87	09 18 30.3	-12 15 40
A907	0.150	3205	47.70	ACIS-I	5.46	09 58 21.1	-11 03 22
A963	0.206	903	36.76	ACIS-S	1.40	10 17 13.9	+39 01 31
A1060	0.012	2220	32.32	ACIS-I	4.79	10 36 51.3	-27 31 35
A1068	0.138	1652	27.17	ACIS-S	1.39	10 40 47.1	+39 57 19
A1201	0.169	4216	40.17	ACIS-S	1.66	11 13 01.1	+13 25 40
A1240	0.159	4961	52.03	ACIS-I	1.98	11 23 32.1	+43 06 32
A1361	0.117	2200	16.96	ACIS-S	2.23	11 43 45.1	+46 21 21
A1413	0.140	537	9.34	ACIS-I	2.05	11 55 18.9	+23 24 31
A1446	0.104	4975	59.12	ACIS-S	1.41	12 01 51.5	+58 01 18
A1569	0.074	6100	41.75	ACIS-I	2.22	12 36 18.7	+16 35 30
A1644	0.047	2206	18.96	ACIS-I	4.97	12 57 14.8	-17 21 13
A1650	0.084	5823	40.13	ACIS-I	1.57	12 58 46.2	-01 45 11
A1651	0.085	4185	9.77	ACIS-I	1.88	12 59 22.9	-04 11 10
A1664	0.128	1648	9.90	ACIS-S	8.91	13 03 41.8	-24 13 06
A1689	0.183	540	10.45	ACIS-I	1.81	13 11 29.5	-01 20 17
A1736	0.046	4186	15.12	ACIS-I	5.38	13 26 52.1	-27 06 33
A1795	0.063	493	19.88	ACIS-S	1.20	13 49 00.5	+26 35 07
A1835	0.253	495	19.77	ACIS-S	2.30	14 01 02.0	+02 51 32
A1914	0.171	542	8.17	ACIS-I	0.93	14 26 03.0	+37 49 32
A1995	0.318	906	58.23	ACIS-S	1.45	14 52 50.4	+58 02 48
A2029	0.077	891	20.07	ACIS-S	3.07	15 10 56.0	+05 44 41
A2034	0.113	2204	54.70	ACIS-I	1.59	15 10 13.1	+33 31 41
A2052	0.035	890	37.23	ACIS-S	2.78	15 16 45.5	+07 00 01
A2063	0.035	6263	17.04	ACIS-S	2.98	15 23 01.8	+08 38 22
A2065	0.073	3182	50.09	ACIS-I	2.94	15 22 42.6	+27 43 21
A2124	0.065	3238	19.61	ACIS-S	1.68	15 44 59.3	+36 03 40
A2142	0.091	1228	12.26	ACIS-S	4.25	15 58 16.1	+27 13 29
A2147	0.035	3211	18.12	ACIS-I	3.40	16 02 17.2	+15 53 43
A2163	0.203	545	9.57	ACIS-I	12.10	16 15 34.1	-06 07 26
A2199	0.030	497	19.72	ACIS-S	0.87	16 28 38.5	+39 33 06
A2204	0.152	499	10.20	ACIS-S	5.66	16 32 45.7	+05 34 43
A2218	0.175	553	5.96	ACIS-I	3.30	16 35 54.0	+66 13 00
A2219	0.225	896	42.84	ACIS-S	1.75	16 40 21.1	+46 41 16
A2244	0.097	4179	57.72	ACIS-S	2.10	17 02 44.0	+34 02 48
A2256	0.058	519	15.00	ACIS-I	4.11	17 03 43.5	+78 43 03
A2319	0.056	3231	14.62	ACIS-I	7.85	19 20 45.3	+43 57 43
A2390	0.228	500	9.96	ACIS-S	6.94	21 53 34.6	+17 40 11
A2462	0.073	4159	39.74	ACIS-S	3.11	22 39 05.2	-17 21 22
A2537	0.295	4962	36.67	ACIS-S	4.50	23 08 16.4	-02 10 44
A2589	0.041	3210	13.86	ACIS-S	4.15	23 24 00.5	+16 49 29
A2597	0.085	922	39.86	ACIS-S	2.50	23 25 18.0	-12 06 30
A2634	0.031	4816	50.16	ACIS-S	5.02	23 38 18.4	+27 01 37
A2657	0.040	4941	16.36	ACIS-I	5.86	23 44 51.0	+09 08 40
A2667	0.230	2214	9.77	ACIS-S	1.64	23 51 47.1	-26 00 18
A2670	0.076	4959	40.14	ACIS-I	2.91	23 54 13.7	-10 25 08
A2717	0.049	6973	47.65	ACIS-I	1.12	00 02 59.4	-36 02 06
A2744	0.308	2212	25.14	ACIS-S	1.60	00 14 19.5	-30 23 19
A3112	0.075	6972	30.16	ACIS-I	2.72	03 17 52.4	-44 14 35
A3158	0.060	3712	31.35	ACIS-I	1.62	03 42 39.6	-53 37 50
A3266	0.059	899	30.14	ACIS-I	1.71	04 31 11.9	-61 24 23
A3376	0.045	3202	44.85	ACIS-I	4.71	06 00 43.6	-40 03 00
A3391	0.051	4943	18.69	ACIS-I	5.58	06 26 15.4	-53 40 52
A3395	0.050	4944	22.17	ACIS-I	6.13	06 27 31.1	-54 23 58
A3526	0.011	504	32.12	ACIS-S	8.07	12 48 51.8	-41 18 21
A3558	0.048	1646	14.61	ACIS-S	3.89	13 27 54.8	-31 29 32
A3562	0.049	4167	19.54	ACIS-I	3.83	13 33 31.8	-31 40 23

Table 1. Continued.

Cluster	z	<i>ObsID</i>	t_{exp} , ks	Instrument	n_H , 10^{20} cm^{-2}	RA(J2000)	DEC(2000)
A3571	0.039	4203	34.44	ACIS-S	3.91	13 47 28.9	-32 51 57
A3667	0.055	889	50.96	ACIS-I	4.95	20 12 30.1	-56 49 00
A3827	0.098	7920	46.17	ACIS-S	2.12	22 01 49.1	-59 57 15
A3921	0.093	4973	29.76	ACIS-I	2.82	22 49 38.6	-64 23 15
A4038	0.030	4992	33.97	ACIS-I	1.54	23 47 37.0	-28 07 42
A4059	0.047	897	41.19	ACIS-S	1.10	23 56 40.7	-34 40 18
AWM4	0.032	9423	75.46	ACIS-S	5.03	16 04 57.0	+23 55 14
CLJ1226.9+3332	0.890	3180	32.12	ACIS-I	1.37	12 26 58.0	+33 32 54
Coma (A1656)	0.023	10672	28.91	ACIS-S	0.93	12 59 48.7	+27 58 50
IIIZw54	0.0311	4182	23.76	ACIS-I	15.50	03 41 17.6	+15 23 44
ISCS J1438+3414	1.41	10461	150.00	ACIS-S	2.01	14 33 22.4	+22 18 35.4
MACSJ0011.7-1523	0.379	3261	22.00	ACIS-I	2.05	00 11 42.9	-15 23 22
MACSJ0159.8-0849	0.405	3265	18.00	ACIS-I	2.08	01 59 48.0	-08 49 00
MACSJ0242.6-2132	0.314	3266	12.00	ACIS-I	2.69	02 42 36.0	-21 32 00
MACSJ0429.6-0253	0.399	3271	24.00	ACIS-I	5.25	04 29 36.0	-02 53 00
MACSJ0647.7+7015	0.59	3196	18.85	ACIS-I	5.63	06 47 45.9	+70 15 03
MACSJ0744.8+3927	0.697	536	19.69	ACIS-I	5.68	07 44 51.8	+39 27 33
MACSJ1115.8+0129	0.355	3275	16.00	ACIS-I	4.39	11 15 53.3	+01 29 47
MACSJ1311.0-0311	0.49	3258	15.00	ACIS-I	1.88	13 11 00.0	-03 11 00
MACSJ1423.8+2404	0.545	4195	113.40	ACIS-I	2.38	14 23 48.3	+24 04 47
MACSJ1427.6-2521	0.318	3279	17.00	ACIS-I	6.18	14 27 39.4	-25 21 02
MACSJ1720.3+3536	0.391	3280	21.00	ACIS-I	3.37	17 20 15.5	+35 36 21
MACSJ1931.8-2635	0.352	3282	14.00	ACIS-I	9.11	19 31 48.0	-26 35 00
MACSJ2129.4-0741	0.589	3199	17.69	ACIS-I	4.84	21 29 26.0	-07 41 28
MACSJ2229.8-2756	0.324	3286	17.00	ACIS-I	1.34	22 29 48.0	-27 56 00
MKW3s	0.045	900	58.03	ACIS-I	3.04	15 21 51.9	+07 42 31
MKW4	0.020	3234	30.36	ACIS-S	1.90	12 03 57.7	+01 53 18
MKW8	0.027	4942	23.45	ACIS-I	2.80	14 40 43.1	+03 27 11
PKS0745-19	0.103	508	28.33	ACIS-S	42.70	07 47 31.32	-19 17 40.0
RXCJ0043.4-2037	0.292	9409	20.18	ACIS-I	1.54	00 43 23.1	-20 37 35
RXCJ0232.2-4420	0.283	4993	23.71	ACIS-I	2.42	02 32 18.7	-44 20 41
RXCJ0307.0-2840	0.253	9414	19.16	ACIS-I	1.36	03 07 01.1	-28 40 30
RXCJ0516.7-5430	0.294	9331	9.64	ACIS-I	6.80	05 16 35.2	-54 16 37
RXCJ0547.6-3152	0.148	9419	20.04	ACIS-I	2.02	05 47 34.2	-31 53 01
RXCJ0605.8-3518	0.141	12899	5.06	ACIS-I	4.47	06 05 52.4	-35 18 22
RXCJ1131.9-1955	0.307	3276	14.10	ACIS-I	4.46	11 32 00.7	-19 53 34
RXCJ2014.8-2430	0.161	11757	20.18	ACIS-S	7.77	20 14 49.7	-24 30 30
RXCJ2129.6+0005	0.235	552	10.09	ACIS-I	4.29	21 29 37.9	+00 05 39
RXCJ2337.6+0016	0.273	3248	9.31	ACIS-I	3.82	23 37 39.7	+00 17 37
ZwCL1215	0.075	4184	12.22	ACIS-I	1.74	12 17 40.60	+03 39 45.0
RCSJ0224-0002	0.778	4987	90.15	ACIS-S	2.92	02 24 00.0	-00 02 00
RCSJ0439-2904	0.951	3577	77.17	ACIS-S	2.63	04 39 38.0	-29 04 55
RCSJ1107-0523	0.735	5825	50.12	ACIS-S	4.24	11 07 22.80	-05 23 49.0
RCSJ1419.2+5326	0.64	3240	10.03	ACIS-S	1.18	14 19 12.0	+53 26 00
RCSJ1620+2929	0.87	3241	37.13	ACIS-S	2.72	16 20 09.40	+29 29 26.0
RCSJ2156+0123	0.335	674	45.76	ACIS-S	2.56	15 47 34.2	+26 38 29.0
RCSJ2318+0034	0.78	4938	51.12	ACIS-S	4.13	23 18 30.67	+00 34 03.0
RCSJ2319+0038	0.904	5750	21.18	ACIS-S	4.16	23 19 53.00	+00 38 00.0
RXJ0439.0+0520	0.208	527	9.71	ACIS-I	10.50	04 39 02.2	+05 20 43
RXJ0848.7+4456	0.570	927	126.74	ACIS-I	2.66	08 48 47.2	+44 56 17
RXJ0849+4452	1.26	945	128.45	ACIS-I	2.50	08 53 43.6	+35 45 53.8
RXJ0910+5422	1.106	2227	84.20	ACIS-I	2.35	09 10 45.36	+54 22 07.3
RXJ1113.1-2615	0.730	915	105.95	ACIS-I	5.47	11 13 05.2	-26 15 26
RXJ1221.4+4918	0.700	1662	80.13	ACIS-I	1.45	12 21 24.5	+49 18 13

cluster. DSDEPROJ is the deprojection routine which assumes only spherical geometry, and solves some of the issues inherent to model-dependent deprojection routines. DSDEPROJ produces a set of “deprojected spectra” which can then be fitted by a suitable spectral model in Xspec. We have shown that this method does not generate the oscillating temperature profiles for multi-temperature clusters and produces a stable solution for an elongated cluster and clusters with breaks in temperature or density.⁵

For each ring we determined the temperature, kT , and the parameter $norm \sim \int n_e n_H dV$ which is proportional to

the electron, n_e and hydrogen, n_H , concentrations. Note, that the other parameters of model were fixed. Using these parameters, we have built the surface brightness profiles which fitted our theoretical surface profiles and then it was used to obtain the mass of each cluster (see below). The surface brightness profiles are measured in the 0.5-7 keV energy band, which provides an optimal ratio of the cluster and background flux in Chandra data.

Note, that for lower redshift clusters in our sample, the statistical accuracy of the surface brightness at large radii is limited mostly by the Chandra field of view.

⁵ The DSDEPROJ source code is available at www-xray.ast.cam.ac.uk/papers/dsdeproj.

3 METHODS

3.1 Galaxy clusters mass profile

In order to calculate the total mass profiles of galaxy clusters, spherical symmetry and hydrostatic equilibrium of clusters was assumed. Similarly to SA07, we modeled the total mass profile as composed of three components: the dark matter halo, the gaseous component and the optically luminous mass of the central cD galaxy.

For the density profile of DM, we used the NFW model having a DM matter content within a fixed radius given by

$$M(< r) = 4\pi\rho_0 r_s^3 \left[\ln\left(1 + \frac{r}{r_s}\right) - \frac{r}{r_s + r} \right]. \quad (4)$$

The gravitational potential ϕ of dark matter can be calculated by the formula

$$\frac{d\phi}{dr} = G \frac{M(< r)}{r^2}. \quad (5)$$

We made all the computations assuming the hydrostatic equilibrium condition of the X-ray emitting gas and wrote the hydrostatic equilibrium condition as follows

$$\nabla P = -\rho_g \nabla \phi(r), \quad (6)$$

where P and ρ_g are the gas pressure and the density, respectively. Since the density and pressure of hot gas have very low values, we can use the ideal gas law, $P = \frac{\rho_g k T_g(r)}{\mu m_p}$, where μ is molecular weight, and m_p the proton mass. We then obtained the equation for unknown gas density distribution

$$\frac{\nabla \rho_g}{\rho_g} = -\nabla \phi(r) \frac{\mu m_p}{k T_g(r)}. \quad (7)$$

For the construction of a hot gas density scalar field of galaxy clusters, we had to calculate numerically the system of the following differential equations

$$\frac{1}{\rho_g} \frac{\partial \rho_g}{\partial x_i} = -\frac{\mu m_p}{k T_g(r)} \frac{\partial \phi(r)}{\partial x_i}, \quad (8)$$

for gas distribution, where $x_i = (x, y, z)$ are the Cartesian coordinates, and then for total mass

$$M(< r) = -(kT(r)r/G\mu m_p) \left(\frac{d \ln \rho}{d \ln r} + \frac{d \ln T}{d \ln r} \right). \quad (9)$$

In case of a single spherically-symmetric galaxy clusters, it is possible to calculate gas density and surface brightness profile analytically, like in the works of Humphrey et al. (2006) and O'Sullivan et al. (2007), for example. We performed the numerical integrations of Eq. (8) and Eq. (9) by means of the Euler method. The integration step was chosen in order to obtain the maximum error of resulting X-ray brightness not bigger than 0.1 per cent.

3.1.1 Modeling of hot gas emission

After 3D reconstruction of gas density field of pair, we were able to obtain the surface brightness in X-ray energy band. The emission flux, that comes from the observed regions, is proportional to the square of the integral density of hot gas, ρ_g^2 , along the line of sight. We used the metal abundance of 0.3 and took $n_e/n_p = 1.17$ and $\rho_g = 1.35 m_p n_p$, where n_e and n_p are the electron and proton concentrations, respectively (Vikhlinin et al. (1999)). We have to note that from

the model, we can obtain the gas density with precision of some constant factor a which depends on the integration boundary conditions of Eq. (8). Therefore the real density ρ_g^{real} of gas is equal to $\rho_g^{real} = a \cdot \rho_g^{sim}$, where ρ_g^{sim} is the density of gas obtained solving the previous differential equations, that we indicate with *sim* standing for simulations. So, we can write $\rho_g^{sim} \equiv \rho_g$ in Eq. (8). Thus the value of emission measure EM_{sim} from simulations can be found as

$$EM_{sim} = \int n_e n_p dV = 0.64/m_p^2 \int (\rho_g^{sim})^2 dV. \quad (10)$$

Using equation (10), we found the next expression

$$norm_{sim} = EM_{sim} \cdot 10^{-14} / [4\pi(D_A(1+z))^2], \quad (11)$$

where D_A is the angular distance to cluster. From the observational data we got the normalization parameter of the best-fit MEKAL model $norm_{MEKAL}$ which was fitted by the $norm_{sim}$ values from the simulations. Since $norm_{MEKAL}$ parameter can be expressed by

$$norm_{MEKAL} = \frac{0.64}{m_p^2} \int \frac{(\rho_g^{real})^2 dV \cdot 10^{-14}}{[4\pi(D_A(1+z))^2]}, \quad (12)$$

from Eq. (10, 11) and Eq. (12), we have found the normalization factor a as

$$a = \sqrt{\frac{norm_{MEKAL}}{norm_{sim}}}. \quad (13)$$

Therefore we able to obtain the field of hot gas density $\rho_g^{real} = a \cdot \rho_g^{sim}$ and emission measure EM_{real} putting into 10 ρ_g^{real} instead of ρ_g^{sim} .

For each cluster we made the series of numerical simulations of the surface brightness profile reconstruction. In our model we used two free parameters ρ_0 and r_s from NFW model. Sorting them out in the acceptable ranges, we selected such pair of values which is the best convenient for describing the observational cluster profile. Using the χ^2 test we found the area of values ρ_0 and r_s with 68% confidence level.

3.1.2 Stellar component

Our sample includes clusters, which have a single, optically dominant cD galaxy near their centers, and the mass of the stars in the central galaxy was accounted through the Jaffe model (Jaffe 1983) with same parameters as in SA07. We assumed, as SA07 a mass of $1.14 \times 10^{12} M_\odot$ for the stellar mass of each central galaxy in the sample.

3.1.3 Best-fit

All computations were made using χ^2 -test

$$\chi^2 = \sum_N \left(\frac{V_{obs} - V_{model}}{\sigma_{obs}} \right)^2, \quad (14)$$

where V_{obs} and V_{model} are the observed and modeled values, respectively. The regions with residual substructure, noticed by SA07, were down-weighted in the mass analysis, similarly to SA07.

3.1.4 Mass profiles scaling

Density profiles of DM are approximatively universal on a large mass scale (Navarro, Frenk, & White 1995; Navarro, Frenk, & White 1996).⁶

In our work we scaled mass profiles with R_{200} and M_{200} (here R_{200} is the radius within which the mean halo density is 200 times the critical density, and M_{200} is the total mass of galaxy cluster inside a sphere with radius R_{200}).

The total mass within a given overdensity Δ is defined in the present work as

$$M_{\Delta} = \frac{4}{3}\pi\Delta\rho_{critical}R_{\Delta}^3, \quad (15)$$

where, as seen in the Introduction, $R_{\Delta}^3 = c_{\Delta}r_s$ is the radius within which the mean cluster overdensity is Δ times $\rho_{critical}$ and the relation with the concentration c_{Δ} and the scale radius r_s holds by definition of the NFW mass profile. In the present paper, we assumed $\Delta = 200$.

An important issue that we are dealing with in this paper, is to understand if the baryonic content in the clusters has influences on the slope of the density profile. To this aim, for each object we calculated the fraction M_b/M_{200} . The quoted ratio M_b/M_{200} will be obtained subtracting from the total mass the DM mass in each cluster. So, the baryonic fraction will be derived as

$$M_b = \frac{800\pi}{3}\rho_{critical} [R_{200,DM+b}^3 - R_{200,DM}^3]. \quad (16)$$

We will then plot the obtained values of α , namely the fit to DM component through a gNFW model, versus the baryonic content M_b .

4 RESULTS

In this section we show and discuss the results for the total mass profiles, the DM profiles, the mass-concentration relation, and the inner slope of the DM profile.

4.1 Total mass profile

In Tab. 2, we summarized the results obtained from modeling the total mass profiles with a NFW model ($\alpha = 1$), similarly to SA07. We plotted just the result concerning the NFW fit and discard the singular isothermal sphere (SI) ($\rho(r) \propto r^{-2}$) since the result of the comparison to the total mass profile with a NFW mode and that with a SI is similar to SA07. The first column includes the names of galaxy cluster studied, the second column the parameter r_s , the third $c_{200} = R_{200}/r_s$, the fourth shows the value of R_{200} , the fifth includes the value of total mass at R_{200} , and the sixth shows the goodness of fit ($\chi^2/\text{d.o.f.}$). Confidence limits are 68 per cent. For most clusters the NFW model is a good fit, similarly to SA07.

⁶ As previously reported, more recent simulations (e.g., Power et al. 2003, Hayashi et al. 2004, and Navarro et al. 2004, Navarro et al. 2004; Stadel et al. 2009) showed that density profiles are better fitted by the Einasto profile.

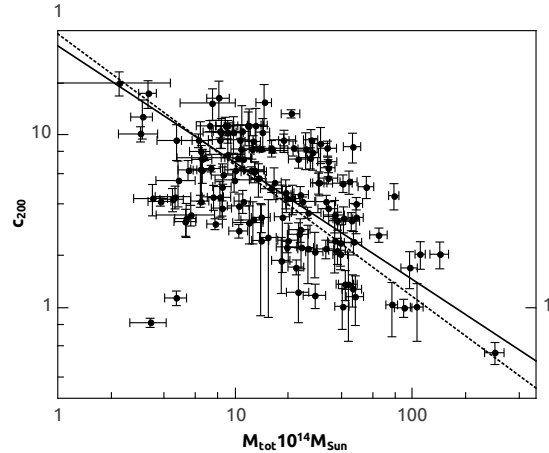


Figure 3. The mass-concentration relation for the total mass (c_{200} - M_{200}). Solid line: best-fitting model with $c_0 = 6.83 \pm 0.64$ and $a = -0.19 \pm 0.07$ ($b = 1$ fixed) for model 19. Dashed line: best-fitting model with $c_0 = 7.73 \pm 1.07$, $a = -0.56 \pm 0.15$ and $b = 0.80 \pm 0.25$ for model 20 (both have 68 per cent confidence level).

4.2 Dark matter profile

In Tab. 3, we summarize the result from the analysis in which cluster mass distributions were separated in DM halo (fitted with a gNFW model), the X-ray emitting halo, and the luminous mass of the BCG.

We considered as SA07 two cases. In the first case, we examined models in which the inner slope of the DM profile was fixed at $\alpha = 1$, corresponding to the NFW model, and in the second, we decomposed the total mass in its DM, diffused gas, and BCG, component (see Sect. 4.3). Again, except some cases, the NFW model provides a good fit to the DM profiles in clusters.

We also calculated the concentration parameter for each cluster and this was used to obtain the mass-concentration parameter. This was done calculating $c_{vir} \equiv c_{200}$ and $M_{vir} \equiv M_{200}$ ⁷ where

$$M_{200} = \frac{4}{3}\pi 200\rho_{critical}R_{200}^3 \quad (18)$$

As in SA07, we define the concentration parameters as $c_{vir} = (r_{vir}^{total}/r_s^{dark})^8$.

The mass-concentration relation measured from the Chandra, shown in Fig. 3, shows that the mass-concentration relation decreases when mass increases. The simplest analytic form that describe the mass-concentration relation is a power-law model (Dolag et al. 2004)

$$c(z) = \frac{c_0}{1+z} \left(\frac{M}{8 \times 10^{14} h^{-1} M_{\odot}} \right)^a. \quad (19)$$

⁷ Note that in SA07 c_{vir} , and M_{vir} are connected through

$$M_{vir} = \frac{4}{3}\pi r_{vir}^3 \Delta_c(z) \rho_{critical} \quad (17)$$

Shaw et al. (2006), with $\Delta_c = 178\Omega_m(z)^{0.45}$ (Lahav et al. 1991)

⁸ Both virial radii and virial masses are calculated for the total mass model, including all mass components.

Table 2. The list of results from modeling the total mass profiles with Navarro-Frenk-White model with slope $\alpha = 1$. First column includes names of galaxy cluster, second shows the r_s parameter from NFW model, third shows the concentration parameter $c_{200} = R_{200}/R_s$ for the NFW model, fourth shows the radius within which the matter density is 200 times the critical density for total and dark matter profiles (in Mpc), fifth and sixth demonstrate the total mass in clusters at radius R_{200} and $\chi^2/\text{d.o.f.}$ goodness of fit. Confidence limits are 68 per cent.

Name	Total mass (dark matter+gas+galaxies)				
	r_s Mpc	NFW profile ($\alpha=1$) c_{200}	R_{200} Mpc	M_{200} $10^{14} M_{\odot}$	$\chi^2/\text{d.o.f.}$
A85	0.76 ^{+0.15} _{-0.17}	3.55 ^{+0.26} _{-0.22}	2.71 ^{+0.65} _{-0.73}	25.68 ^{+4.89} _{-3.18}	2.31
A119	0.64 ^{+0.23} _{-0.22}	4.12 ^{+0.25} _{-0.23}	2.66 ^{+0.13} _{-0.15}	24.06 ^{+4.16} _{-2.18}	1.57
A133	0.29 ^{+0.15} _{-0.05}	8.11 ^{+0.25} _{-0.26}	2.33 ^{+0.19} _{-0.12}	16.34 ^{+3.55} _{-2.17}	1.37
A168	0.24 ^{+0.12} _{-0.10}	7.37 ^{+0.26} _{-0.27}	1.74 ^{+0.45} _{-0.56}	6.74 ^{+2.03} _{-1.78}	2.11
A209	0.65 ^{+0.18} _{-0.21}	3.11 ^{+0.77} _{-0.67}	2.01 ^{+0.54} _{-0.67}	12.05 ^{+2.34} _{-2.11}	1.03
A262	0.13 ^{+0.07} _{-0.06}	10.11 ^{+1.02} _{-0.98}	1.33 ^{+0.12} _{-0.09}	2.93 ^{+0.73} _{-0.67}	1.35
A383	0.46 ^{+0.16} _{-0.17}	3.44 ^{+0.47} _{-0.36}	1.57 ^{+0.21} _{-0.17}	5.63 ^{+2.04} _{-1.19}	2.02
A399	1.43 ^{+0.28} _{-0.36}	2.15 ^{+0.37} _{-0.33}	3.07 ^{+1.37} _{-1.36}	37.90 ^{+3.94} _{-4.11}	2.47
A401	0.96 ^{+0.36} _{-0.37}	3.19 ^{+0.38} _{-0.33}	3.07 ^{+1.21} _{-0.99}	37.97 ^{+4.16} _{-2.81}	2.47
A478	0.58 ^{+0.26} _{-0.21}	4.51 ^{+0.31} _{-0.48}	2.60 ^{+0.41} _{-0.55}	23.35 ^{+2.62} _{-2.17}	0.84
A496	0.17 ^{+0.09} _{-0.06}	11.26 ^{+0.83} _{-0.81}	1.93 ^{+0.48} _{-0.35}	9.10 ^{+1.19} _{-1.27}	0.92
A521	0.15 ^{+0.03} _{-0.04}	11.26 ^{+0.83} _{-0.78}	1.67 ^{+0.16} _{-0.12}	7.21 ^{+1.16} _{-1.19}	1.29
A539	0.18 ^{+0.05} _{-0.04}	10.37 ^{+2.04} _{-2.01}	1.88 ^{+0.33} _{-0.18}	8.38 ^{+1.46} _{-1.77}	3.32
A576	0.59 ^{+0.16} _{-0.17}	4.28 ^{+0.83} _{-0.81}	2.55 ^{+0.56} _{-0.73}	21.11 ^{+2.16} _{-1.19}	1.03
A644	1.33 ^{+0.43} _{-0.29}	2.19 ^{+0.25} _{-0.27}	2.92 ^{+0.77} _{-0.81}	32.55 ^{+3.51} _{-2.99}	1.05
A697	0.36 ^{+0.12} _{-0.13}	5.58 ^{+1.11} _{-1.22}	2.04 ^{+0.18} _{-0.22}	13.56 ^{+1.27} _{-1.14}	4.32
A754	3.08 ^{+0.39} _{-0.48}	1.02 ^{+0.22} _{-0.22}	3.15 ^{+1.26} _{-1.15}	40.30 ^{+3.71} _{-3.16}	1.38
A773	0.63 ^{+0.11} _{-0.13}	3.33 ^{+0.61} _{-0.53}	2.11 ^{+0.26} _{-0.35}	14.09 ^{+1.72} _{-1.28}	1.77
A907	0.27 ^{+0.06} _{-0.08}	6.25 ^{+1.01} _{-0.89}	1.67 ^{+0.15} _{-0.21}	6.54 ^{+0.73} _{-0.72}	1.38
A963	0.41 ^{+0.15} _{-0.13}	4.35 ^{+1.01} _{-0.99}	1.77 ^{+0.14} _{-0.18}	8.22 ^{+1.24} _{-0.91}	2.83
A1060	0.19 ^{+0.07} _{-0.03}	10.27 ^{+2.45} _{-2.17}	1.99 ^{+0.36} _{-0.34}	9.81 ^{+1.32} _{-1.16}	2.16
A1068	0.58 ^{+0.19} _{-0.11}	3.05 ^{+0.21} _{-0.22}	1.77 ^{+0.14} _{-0.06}	7.71 ^{+0.71} _{-0.78}	1.04
A1201	0.25 ^{+0.11} _{-0.10}	6.27 ^{+0.83} _{-0.81}	1.56 ^{+0.51} _{-0.48}	5.43 ^{+0.59} _{-0.66}	1.22
A1240	0.27 ^{+0.08} _{-0.10}	6.38 ^{+0.28} _{-0.15}	1.73 ^{+0.66} _{-0.58}	7.34 ^{+0.94} _{-0.81}	1.11
A1361	0.28 ^{+0.04} _{-0.08}	7.28 ^{+0.83} _{-0.81}	2.01 ^{+0.84} _{-0.81}	11.07 ^{+1.34} _{-1.18}	1.00
A1413	0.31 ^{+0.14} _{-0.10}	5.85 ^{+0.67} _{-0.44}	1.83 ^{+0.66} _{-0.57}	8.53 ^{+1.18} _{-0.92}	1.99
A1446	0.23 ^{+0.05} _{-0.03}	9.16 ^{+0.67} _{-0.72}	2.11 ^{+0.48} _{-0.43}	12.66 ^{+1.26} _{-1.15}	1.37
A1569	0.21 ^{+0.03} _{-0.04}	10.37 ^{+2.01} _{-2.04}	2.22 ^{+0.84} _{-0.81}	14.35 ^{+1.34} _{-1.11}	1.12
A1644	0.15 ^{+0.04} _{-0.08}	15.35 ^{+3.89} _{-4.17}	2.25 ^{+0.39} _{-0.36}	14.60 ^{+1.47} _{-1.17}	4.11
A1650	1.52 ^{+0.33} _{-0.29}	2.03 ^{+0.35} _{-0.37}	3.10 ^{+0.72} _{-0.73}	39.44 ^{+3.74} _{-2.78}	1.22
A1651	0.57 ^{+0.16} _{-0.17}	4.29 ^{+0.74} _{-0.71}	2.45 ^{+0.46} _{-0.37}	19.48 ^{+2.45} _{-2.17}	1.28
A1664	0.35 ^{+0.11} _{-0.14}	7.24 ^{+0.83} _{-0.81}	2.55 ^{+0.72} _{-0.77}	22.84 ^{+2.81} _{-2.19}	1.66
A1689	0.27 ^{+0.05} _{-0.05}	8.35 ^{+0.81} _{-0.85}	2.23 ^{+0.73} _{-0.07}	16.09 ^{+2.81} _{-1.73}	1.54
A1736	0.11 ^{+0.00} _{-0.01}	16.27 ^{+4.16} _{-4.13}	1.85 ^{+0.42} _{-0.37}	8.11 ^{+1.15} _{-1.18}	4.33
A1795	0.53 ^{+0.20} _{-0.21}	4.61 ^{+0.55} _{-0.88}	2.46 ^{+0.36} _{-0.54}	19.34 ^{+2.18} _{-2.16}	1.33
A1835	0.92 ^{+0.18} _{-0.27}	2.66 ^{+0.35} _{-0.44}	2.45 ^{+0.31} _{-0.24}	22.86 ^{+2.86} _{-3.11}	2.77
A1914	3.62 ^{+0.48} _{-0.37}	1.04 ^{+0.36} _{-0.33}	3.77 ^{+0.76} _{-0.67}	76.85 ^{+5.81} _{-5.28}	3.28
A1995	0.95 ^{+0.33} _{-0.28}	3.17 ^{+0.38} _{-0.33}	3.01 ^{+0.43} _{-0.42}	45.32 ^{+5.16} _{-3.18}	2.22
A2029	0.42 ^{+0.17} _{-0.19}	6.99 ^{+0.41} _{-0.43}	2.94 ^{+0.96} _{-0.82}	33.43 ^{+3.71} _{-4.12}	1.20
A2034	0.99 ^{+0.17} _{-0.15}	2.46 ^{+0.59} _{-0.62}	2.45 ^{+0.51} _{-0.50}	19.98 ^{+2.54} _{-1.37}	1.38
A2052	0.19 ^{+0.03} _{-0.04}	10.33 ^{+1.39} _{-1.33}	1.93 ^{+0.55} _{-0.61}	9.12 ^{+1.26} _{-1.72}	1.32
A2063	0.27 ^{+0.14} _{-0.10}	7.36 ^{+0.38} _{-0.33}	2.01 ^{+0.45} _{-0.37}	10.30 ^{+1.94} _{-1.29}	1.92
A2065	1.31 ^{+0.21} _{-0.18}	2.38 ^{+0.64} _{-0.56}	3.11 ^{+0.46} _{-0.37}	39.43 ^{+5.82} _{-4.18}	1.20
A2124	0.19 ^{+0.04} _{-0.02}	11.36 ^{+2.84} _{-2.81}	2.16 ^{+0.63} _{-0.61}	13.12 ^{+1.37} _{-1.27}	1.47
A2142	0.54 ^{+0.13} _{-0.10}	5.27 ^{+0.83} _{-0.79}	2.82 ^{+0.59} _{-0.61}	29.87 ^{+2.47} _{-3.17}	2.29
A2147	0.20 ^{+0.02} _{-0.03}	10.46 ^{+3.81} _{-4.27}	2.05 ^{+0.14} _{-0.17}	10.93 ^{+1.27} _{-1.28}	1.28
A2163	2.07 ^{+0.37} _{-0.35}	2.04 ^{+0.37} _{-0.33}	4.22 ^{+0.68} _{-0.66}	111.18 ^{+5.92} _{-7.38}	1.75
A2199	0.34 ^{+0.09} _{-0.10}	6.27 ^{+0.25} _{-0.26}	2.14 ^{+0.28} _{-0.19}	12.38 ^{+2.18} _{-1.29}	1.17
A2204	0.90 ^{+0.11} _{-0.07}	2.83 ^{+0.32} _{-0.44}	2.55 ^{+0.71} _{-0.66}	23.35 ^{+3.16} _{-2.17}	1.28
A2218	0.26 ^{+0.01} _{-0.03}	6.33 ^{+2.34} _{-1.23}	1.65 ^{+0.16} _{-0.12}	6.46 ^{+0.82} _{-0.83}	1.10
A2219	0.84 ^{+0.15} _{-0.17}	3.44 ^{+0.73} _{-0.73}	2.89 ^{+0.78} _{-0.91}	36.49 ^{+4.32} _{-3.39}	2.18
A2244	1.24 ^{+0.15} _{-0.17}	2.43 ^{+0.84} _{-0.81}	3.01 ^{+0.51} _{-0.39}	36.52 ^{+3.16} _{-3.18}	4.19
A2256	2.87 ^{+0.44} _{-0.37}	1.16 ^{+0.37} _{-0.27}	3.33 ^{+0.62} _{-0.58}	47.78 ^{+5.37} _{-5.29}	2.11

Table 2. Continued.

Name	Total mass (dark matter+gas+galaxies)					$\chi^2/\text{d.o.f.}$
	NFW profile ($\alpha=1$)		R_{200} Mpc	M_{200} $10^{14} M_{\odot}$		
	r_s Mpc	c_{200}				
A2319	$2.57^{+0.32}_{-0.19}$	$1.28^{+0.27}_{-0.22}$	$3.29^{+1.12}_{-1.29}$	$46.00^{+4.57}_{-5.82}$	1.22	
A2390	$1.26^{+0.16}_{-0.16}$	$2.11^{+0.52}_{-0.62}$	$2.65^{+0.61}_{-0.54}$	$28.21^{+3.15}_{-2.39}$	1.02	
A2462	$0.19^{+0.03}_{-0.06}$	$13.23^{+0.72}_{-0.67}$	$2.51^{+0.27}_{-0.22}$	$20.73^{+2.47}_{-2.49}$	1.05	
A2537	$0.44^{+0.12}_{-0.14}$	$4.88^{+0.24}_{-0.24}$	$2.15^{+0.53}_{-0.55}$	$16.12^{+2.16}_{-2.19}$	1.66	
A2589	$0.32^{+0.09}_{-0.06}$	$6.27^{+0.75}_{-0.72}$	$1.99^{+0.63}_{-0.51}$	$10.05^{+1.27}_{-1.29}$	1.48	
A2597	$0.24^{+0.05}_{-0.03}$	$8.28^{+1.27}_{-1.26}$	$2.01^{+0.57}_{-0.73}$	$10.76^{+1.27}_{-1.22}$	2.12	
A2634	$0.18^{+0.05}_{-0.03}$	$11.38^{+2.17}_{-2.16}$	$2.11^{+0.05}_{-0.11}$	$11.88^{+2.15}_{-1.27}$	1.47	
A2657	$0.36^{+0.11}_{-0.10}$	$5.49^{+0.83}_{-0.81}$	$1.98^{+0.15}_{-0.11}$	$9.89^{+2.17}_{-1.28}$	1.55	
A2667	$1.04^{+0.23}_{-0.15}$	$2.25^{+0.17}_{-0.15}$	$2.35^{+0.45}_{-0.38}$	$19.71^{+2.61}_{-1.55}$	1.28	
A2670	$0.44^{+0.13}_{-0.16}$	$5.33^{+1.11}_{-1.09}$	$2.33^{+0.38}_{-1.02}$	$16.62^{+1.55}_{-1.62}$	2.21	
A2717	$0.35^{+0.05}_{-0.04}$	$6.12^{+0.84}_{-0.81}$	$2.16^{+0.79}_{-0.81}$	$12.94^{+2.11}_{-1.26}$	1.83	
A2744	$1.38^{+0.30}_{-0.27}$	$1.72^{+0.15}_{-0.17}$	$2.38^{+0.36}_{-0.31}$	$22.17^{+2.14}_{-2.26}$	1.36	
A3112	$0.26^{+0.04}_{-0.03}$	$9.36^{+0.73}_{-0.73}$	$2.43^{+0.31}_{-0.26}$	$18.84^{+3.14}_{-2.16}$	3.27	
A3158	$1.24^{+0.13}_{-0.14}$	$2.19^{+0.80}_{-0.81}$	$2.71^{+0.38}_{-0.62}$	$25.80^{+3.17}_{-2.72}$	3.22	
A3266	$0.35^{+0.05}_{-0.05}$	$8.36^{+0.83}_{-0.81}$	$2.95^{+0.52}_{-0.77}$	$33.25^{+4.16}_{-3.27}$	3.21	
A3376	$0.37^{+0.03}_{-0.04}$	$7.38^{+1.01}_{-1.03}$	$2.75^{+0.43}_{-0.62}$	$26.61^{+3.72}_{-2.91}$	1.29	
A3391	$0.26^{+0.05}_{-0.03}$	$9.26^{+1.14}_{-1.36}$	$2.45^{+0.84}_{-0.35}$	$18.91^{+1.25}_{-1.28}$	1.02	
A3395	$0.79^{+0.11}_{-0.10}$	$3.74^{+0.35}_{-0.37}$	$2.97^{+0.96}_{-0.84}$	$33.67^{+4.27}_{-4.12}$	1.07	
A3526	$0.18^{+0.04}_{-0.03}$	$10.43^{+0.81}_{-0.83}$	$1.88^{+0.25}_{-0.27}$	$8.26^{+0.72}_{-0.28}$	1.66	
A3558	$0.30^{+0.04}_{-0.07}$	$8.37^{+0.78}_{-0.83}$	$2.55^{+0.38}_{-0.36}$	$21.27^{+3.27}_{-2.16}$	2.33	
A3562	$0.27^{+0.05}_{-0.06}$	$8.26^{+0.25}_{-0.27}$	$2.22^{+0.15}_{-0.17}$	$14.05^{+1.56}_{-1.46}$	2.17	
A3571	$0.32^{+0.06}_{-0.06}$	$8.92^{+1.98}_{-1.19}$	$2.88^{+0.46}_{-0.37}$	$30.41^{+3.75}_{-3.84}$	1.36	
A3667	$0.29^{+0.09}_{-0.04}$	$9.36^{+1.19}_{-1.36}$	$2.75^{+0.61}_{-0.52}$	$26.84^{+3.88}_{-2.46}$	1.22	
A3827	$0.87^{+0.09}_{-0.13}$	$4.45^{+0.67}_{-0.77}$	$3.89^{+0.16}_{-0.43}$	$78.90^{+5.26}_{-4.27}$	1.02	
A3921	$0.53^{+0.08}_{-0.07}$	$5.27^{+0.73}_{-0.71}$	$2.81^{+0.33}_{-0.26}$	$29.61^{+2.15}_{-1.77}$	1.33	
A4038	$0.20^{+0.02}_{-0.01}$	$9.38^{+1.03}_{-1.01}$	$1.87^{+0.25}_{-0.17}$	$8.26^{+1.18}_{-0.92}$	1.32	
A4059	$0.22^{+0.02}_{-0.00}$	$9.36^{+2.02}_{-2.01}$	$2.03^{+0.28}_{-0.34}$	$10.72^{+0.92}_{-1.28}$	1.37	
AWM4	$0.24^{+0.03}_{-0.02}$	$7.21^{+1.02}_{-1.03}$	$1.73^{+0.27}_{-0.22}$	$6.55^{+0.85}_{-0.37}$	1.22	
CLJ1226.9+3332	$1.75^{+0.13}_{-0.11}$	$2.04^{+0.32}_{-0.36}$	$3.57^{+0.51}_{-0.52}$	$143.19^{+15.26}_{-17.26}$	1.45	
Coma (A1656)	$2.35^{+0.43}_{-0.55}$	$1.37^{+0.25}_{-0.27}$	$3.22^{+0.59}_{-0.62}$	$41.94^{+4.72}_{-3.92}$	1.44	
II Zw54	$0.17^{+0.01}_{-0.02}$	$11.25^{+1.33}_{-1.38}$	$1.91^{+0.51}_{-0.43}$	$8.81^{+1.04}_{-0.93}$	1.66	
ISCS J1438.1+3414	$6.81^{+0.55}_{-0.72}$	$0.55^{+0.05}_{-0.08}$	$3.75^{+0.33}_{-0.38}$	$293.15^{+18.27}_{-36.84}$	1.73	
MACSJ0011.7-1523	$0.75^{+0.13}_{-0.23}$	$4.01^{+0.23}_{-0.33}$	$3.01^{+0.30}_{-0.31}$	$48.34^{+3.82}_{-4.15}$	1.43	
MACSJ0159.8-0849	$0.54^{+0.12}_{-0.13}$	$5.35^{+0.82}_{-0.72}$	$2.89^{+0.51}_{-0.52}$	$44.00^{+4.84}_{-4.44}$	1.49	
MACSJ0242.6-2132	$0.32^{+0.06}_{-0.04}$	$7.88^{+1.64}_{-1.23}$	$2.55^{+0.46}_{-0.45}$	$27.44^{+1.99}_{-2.19}$	1.33	
MACSJ0429.6-0253	$0.65^{+0.13}_{-0.10}$	$3.36^{+1.76}_{-1.65}$	$2.17^{+0.78}_{-0.84}$	$18.50^{+1.82}_{-1.63}$	1.38	
MACSJ0647.7+7015	$3.42^{+0.35}_{-0.36}$	$1.00^{+0.12}_{-0.11}$	$3.42^{+0.45}_{-0.54}$	$89.51^{+10.14}_{-9.28}$	1.22	
MACSJ0744.8+3927	$3.44^{+0.39}_{-0.37}$	$1.01^{+0.37}_{-0.16}$	$3.48^{+0.45}_{-0.47}$	$106.48^{+8.82}_{-6.18}$	1.28	
MACSJ1115.8+0129	$1.07^{+0.09}_{-0.11}$	$2.23^{+0.53}_{-0.55}$	$2.39^{+0.64}_{-0.63}$	$23.59^{+4.17}_{-3.18}$	3.21	
MACSJ1311.0-0311	$0.60^{+0.07}_{-0.06}$	$5.01^{+0.73}_{-0.35}$	$3.02^{+0.33}_{-0.35}$	$55.11^{+4.84}_{-5.58}$	2.18	
MACSJ1423.8+2404	$0.85^{+0.29}_{-0.22}$	$3.33^{+0.63}_{-0.63}$	$2.83^{+0.17}_{-0.32}$	$48.21^{+4.72}_{-4.72}$	1.88	
MACSJ1427.6-2521	$0.30^{+0.17}_{-0.32}$	$8.28^{+1.99}_{-1.77}$	$2.47^{+0.81}_{-0.84}$	$25.04^{+2.36}_{-2.26}$	2.18	
MACSJ1720.3+3536	$0.54^{+0.10}_{-0.11}$	$5.25^{+0.61}_{-0.36}$	$2.83^{+0.68}_{-0.67}$	$40.70^{+5.17}_{-4.92}$	1.72	
MACSJ1931.8-2635	$0.65^{+0.05}_{-0.06}$	$4.11^{+0.36}_{-0.24}$	$2.67^{+0.91}_{-0.92}$	$32.78^{+3.91}_{-4.19}$	1.44	
MACSJ2129.4-0741	$2.06^{+0.32}_{-0.27}$	$1.70^{+0.38}_{-0.41}$	$3.51^{+0.71}_{-0.72}$	$96.66^{+10.26}_{-10.82}$	1.46	
MACSJ2229.8-2756	$0.35^{+0.06}_{-0.03}$	$8.54^{+1.67}_{-1.36}$	$3.02^{+0.81}_{-0.84}$	$46.06^{+4.82}_{-5.17}$	1.33	
MKW3s	$0.18^{+0.03}_{-0.03}$	$11.37^{+2.18}_{-2.73}$	$2.11^{+0.12}_{-0.18}$	$12.02^{+2.47}_{-3.19}$	1.22	
MKW4	$0.06^{+0.01}_{-0.00}$	$19.93^{+3.15}_{-3.17}$	$1.21^{+0.10}_{-0.14}$	$2.22^{+1.84}_{-2.10}$	1.37	
MKW8	$0.12^{+0.02}_{-0.01}$	$15.28^{+3.14}_{-3.16}$	$1.81^{+0.33}_{-0.28}$	$7.47^{+1.48}_{-2.57}$	1.92	
PKS0745-191	$0.45^{+0.06}_{-0.06}$	$6.45^{+0.73}_{-0.61}$	$2.92^{+0.22}_{-0.18}$	$33.52^{+3.17}_{-3.17}$	1.82	
RXCJ0043.4-2037	$0.19^{+0.03}_{-0.01}$	$8.01^{+3.85}_{-3.03}$	$1.58^{+0.17}_{-0.17}$	$6.38^{+0.82}_{-0.84}$	1.11	
RXCJ0232.2-4420	$1.19^{+0.13}_{-0.16}$	$1.88^{+0.67}_{-0.66}$	$2.25^{+0.34}_{-0.43}$	$18.25^{+2.16}_{-1.82}$	1.22	
RXCJ0307.0-2840	$0.62^{+0.07}_{-0.07}$	$3.22^{+0.88}_{-0.77}$	$2.01^{+0.26}_{-0.29}$	$12.62^{+1.72}_{-1.82}$	1.38	
RXCJ0516.7-5430	$0.83^{+0.09}_{-0.06}$	$2.45^{+1.55}_{-0.77}$	$2.05^{+0.32}_{-0.25}$	$13.96^{+1.54}_{-1.22}$	1.72	
RXCJ0547.6-3152	$0.48^{+0.06}_{-0.07}$	$4.14^{+0.57}_{-0.63}$	$1.99^{+0.14}_{-0.43}$	$11.06^{+1.17}_{-1.10}$	1.34	
RXCJ0605.8-3518	$0.40^{+0.02}_{-0.01}$	$4.14^{+0.33}_{-0.23}$	$1.66^{+0.18}_{-0.15}$	$6.37^{+0.75}_{-0.72}$	1.38	
RXCJ1131.9-1955	$0.83^{+0.11}_{-0.02}$	$2.55^{+1.24}_{-1.67}$	$2.11^{+0.34}_{-0.28}$	$15.43^{+1.45}_{-1.66}$	1.88	

Table 2. Continued.

Name	Total mass (dark matter+gas+galaxies)				$\chi^2/\text{d.o.f.}$
	NFW profile ($\alpha=1$)		R_{200} Mpc	M_{200} $10^{14} M_{\odot}$	
	r_s Mpc	c_{200}			
RXCJ2014.8-2430	$0.50^{+0.07}_{-0.04}$	$3.88^{+0.54}_{-0.67}$	$1.95^{+0.12}_{-0.17}$	$10.53^{+1.48}_{-1.47}$	2.83
RXCJ2129.6+0005	$0.47^{+0.07}_{-0.06}$	$3.77^{+0.38}_{-0.33}$	$1.77^{+0.22}_{-0.21}$	$8.46^{+0.94}_{-1.10}$	2.33
RXCJ2337.6+0016	$0.35^{+0.06}_{-0.03}$	$5.02^{+1.55}_{-1.77}$	$1.75^{+0.22}_{-0.18}$	$8.50^{+1.01}_{-0.89}$	2.18
ZwCL1215	$0.52^{+0.08}_{-0.06}$	$5.62^{+0.42}_{-0.40}$	$2.95^{+0.56}_{-0.63}$	$33.71^{+4.17}_{-4.29}$	1.04
RCSJ0224-0002	$0.56^{+0.09}_{-0.07}$	$2.78^{+0.25}_{-0.25}$	$1.56^{+0.16}_{-0.17}$	$10.51^{+1.11}_{-1.28}$	1.09
RCSJ0439-2904	$0.25^{+0.01}_{-0.03}$	$4.12^{+0.25}_{-0.21}$	$1.04^{+0.14}_{-0.12}$	$3.79^{+0.56}_{-0.27}$	1.20
RCSJ1107-0523	$0.40^{+0.03}_{-0.03}$	$3.15^{+0.56}_{-0.45}$	$1.26^{+0.29}_{-0.27}$	$5.27^{+0.74}_{-0.45}$	1.05
RCSJ1419.2+5326	$0.28^{+0.03}_{-0.05}$	$6.24^{+0.73}_{-0.71}$	$1.76^{+0.28}_{-0.21}$	$12.91^{+1.64}_{-1.72}$	1.48
RCSJ1620+2929	$0.31^{+0.05}_{-0.06}$	$4.38^{+0.72}_{-0.71}$	$1.35^{+0.18}_{-0.17}$	$7.57^{+1.02}_{-1.04}$	1.47
RCS2156+0123	$1.93^{+0.12}_{-0.24}$	$1.23^{+0.41}_{-0.30}$	$2.38^{+0.28}_{-0.29}$	$22.80^{+3.28}_{-2.88}$	1.05
RCSJ2318+0034	$1.83^{+0.13}_{-0.11}$	$1.18^{+0.19}_{-0.17}$	$2.17^{+0.37}_{-0.31}$	$28.37^{+4.11}_{-3.18}$	2.10
RCSJ2319+0038	$0.71^{+0.11}_{-0.09}$	$3.27^{+0.56}_{-0.55}$	$2.34^{+0.48}_{-0.29}$	$40.96^{+4.25}_{-5.22}$	1.36
RXJ0439.0+0520	$0.24^{+0.05}_{-0.03}$	$7.71^{+1.27}_{-1.77}$	$1.83^{+0.48}_{-0.36}$	$9.11^{+1.75}_{-2.27}$	1.46
RXJ0848.7+4456	$1.40^{+0.14}_{-0.17}$	$0.82^{+0.05}_{-0.01}$	$1.15^{+0.15}_{-0.13}$	$3.32^{+0.73}_{-0.77}$	2.66
RXJ0849+4452	$1.89^{+0.27}_{-0.25}$	$1.14^{+0.11}_{-0.10}$	$2.16^{+0.52}_{-0.51}$	$4.67^{+0.66}_{-0.47}$	1.88
RXJ0910+5422	$0.96^{+0.15}_{-0.09}$	$2.64^{+0.25}_{-0.21}$	$2.53^{+0.63}_{-0.63}$	$64.92^{+5.67}_{-7.34}$	1.46
RXJ1113.1-2615	$0.38^{+0.06}_{-0.04}$	$3.28^{+0.73}_{-0.71}$	$1.26^{+0.15}_{-0.11}$	$5.30^{+0.73}_{-0.48}$	1.22
RXJ1221.4+4918	$1.10^{+0.15}_{-0.10}$	$2.39^{+0.37}_{-0.35}$	$2.64^{+0.31}_{-0.35}$	$46.64^{+5.22}_{-3.49}$	1.07

For example, Shaw et al. (2006) by using the previous relation, with their simulated data, found $c_0 = 6.47 \pm 0.03$ and $a = -0.12 \pm 0.03$ for 68 per cent confidence limits in agreement with Eke et al. (2001), and Bullock et al. (2001). In a recent work by Kulinich et al. (2012), a new method to calculate a halo concentration parameter, and taking into account the halo overdensity and merging, was proposed. In our research, we used also a power-law model, obtaining $c_0 = 6.83 \pm 0.64$ and $a = -0.19 \pm 0.07$ ($b = 1$ fixed). As we show in Fig. 3, using the measurements obtained with our method above, the relation between concentration and total masses for CDM halos is represented not so well from Dolag et al. (2004) formula (Eq. 22). In agreement with SA07, Fig. 1, the model with $b = 1$, provides a poor fit for the observations, lying systematically below the data at lower masses and above it in the highest mass range.

In order to improve the description of Chandra data, we assumed, as SA07, differently from Bullock et al. (2001) to model a redshift evolution of the form $(1+z)^{-b}$, with b free

$$c = \frac{c_0}{(1+z)^b} \left(\frac{M_{200}}{8 \times 10^{14} h^{-1} M_{\odot}} \right)^a. \quad (20)$$

The motivation to the new redshift dependence comes from the fact that clusters are more complicated objects than those assumed in Bullock et al. (2001) (see discussion in Sec. 3.2 of Sa07, and Zhao et al. 2003).

The results from a fit using Eq. (20), with c_0 , a and b all free, are shown by the dashed line in Fig. 3. This model provides an improved description of the data with $\chi^2 = 1.3$ and best-fitting parameters $c_0 = 7.73 \pm 1.07$, $a = -0.56 \pm 0.15$ and $b = 0.80 \pm 0.25$ (68 per cent confidence limits). Note, that RXJ0848.7+4456 and RXJ0849+4452 have been excluded from the fitting, since they give small values for concentra-

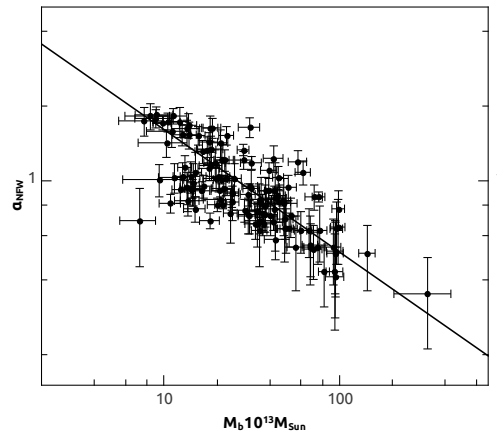


Figure 4. α - M_b relation for all sample of galaxy clusters. The data were obtained fitting the DM profiles of clusters with the gNFW model. The baryonic mass was obtained, as described in the text, by subtracting the DM component from the total mass.

tion parameter (c_{200} , $0.82^{+0.05}_{-0.01}$ and $1.14^{+0.11}_{-0.10}$, respectively).

4.3 The inner slope of DM profiles

Finally, we fitted the DM profiles by means of a gNFW model to have hints on the inner slopes of the density profiles. The results are summarized in Tab. 3. The value of α obtained is $\alpha = 0.94 \pm 0.13$ (68 per cent confidence limits). This result is consistent with CDM predictions.

The values of the slope are in the range $0.5 < \alpha < 1.8$

and for the largest number of clusters the density profile is compatible with the expectation from Λ CDM model $0.7 < \alpha < 1.5$ (SA07). Only some clusters have slopes smaller than 0.7 and they are usually characterized by an higher M_b with respect to clusters with larger α .

4.4 Inner slope and baryons content

As discussed in the introduction not all clusters have profiles best fitted by the NFW model (e.g., Sand et al. 2002, Sand et al. 2004, Sand et al. 2008; Newman et al. 2009, Newman et al. 2011). Among the processes able to produce flat profile, the role of baryons has been several times claimed (see the introduction). Recently, Del Popolo (2012) studied the effect of baryons, and the central BCG in shaping the inner density profile. It was also shown how higher content of baryons can give rise to profiles similar to A611 and A383 which have slopes flatter than NFW profile, and small baryonic content can produce steeper inner profiles in agreement with the NFW model (MACS J1423.8+2404, RXJ1133).

Motivated by the previous arguments, we studied the eventual correlation among the inner density profile slope, α , and the baryonic content of the clusters that we studied.

Similarly to SA07, we performed an analysis in which the total mass was separated in the DM halo, the X-ray emitting halo, and the luminous mass of the BCG (this is the second case mentioned in Sect. 4.2). We fitted the DM profile with a gNFW model and calculated α , and reported the values in Tab. 3. From the analysis the baryonic content, M_b is calculated summing the diffuse gas content and the baryons contained in the central cD galaxy in each cluster. In Fig. 4, we plot the inner slope, α , versus the baryonic content at the radius of R_{200} . A2255 has been excluded during fitting, because this galaxy cluster gave small uncertain value of χ^2 . The plot shows a tight correlation between the inner slope α and the baryonic content: the larger is the baryonic content the flatter is the inner profile. This results is in agreement with studies of the role of baryons on the inner slope of clusters (e.g., Del Popolo 2009, Del Popolo 2012, Romano-Díaz et al. 2008, Romano-Díaz et al. 2009).

An important issue to stress is the fact that we assumed, as SA07 that all the central BCG has the same mass, so that the difference of the baryon content from cluster to cluster is connected to the diffused gas content. The expectation that the central baryonic content is the only or the fundamental contribution to shape the inner density profile is only partly true. To understand this, it is interesting to discuss more in detail the role of the total baryonic mass, M_b , and the central one.

Baryons and the baryon diffused component presence produces in general a flattening of the density profile (El-Zant et al. 2001, El-Zant et al. 2004; Romano-Díaz et al. 2008, Del Popolo 2009, Governato et al. 2010), and rounder halos than those seen in DM simulations (Debattista et al. 2008; Abadi et al. 2010). The final configuration of a cluster is fixed by the initial quantity of baryons present in the proto cluster and by collapse/formation process. Then it is logic to expect that the final central baryonic content and the BCG mass is somehow correlated with baryonic and total cluster mass, M_{cl} . For example, Whiley et al. (2008), found that

$M_{BCG} \propto M_{cl}^{0.4}$ or $M_{cl}^{0.5}$ depending on the feedback model used. Also a correlation between BCG luminosity and cluster X-ray luminosity was found by several authors (Schombert 1988; Edge & Stewart 1991; Edge & Stewart 1991; Hudson & Ebeling 1997). Whiley et al. (2008) measured the quoted correlation as $M_{BCG} \propto M_{cl}^{0.12 \pm 0.03}$ for K band magnitudes inside a diameter of 37 kpc (radius of $13h^{-1}$ kpc). Brough et al. (2008) found $L_{BCG} \propto M_{cl}^{0.11 \pm 0.10}$ at K band inside $12h^{-1}$ kpc (several other results are given in Lin & Mohr 2004; Popesso et al. 2007; Yang et al. 2008; Haarsma et al. 2010; Fedeli 2012). The flattening of the slope can be interpreted as due to the fact that the presence of a larger quantity of baryons guarantees a larger transfer of energy and angular momentum from baryons to DM, with the result that DM moves to larger orbits, reducing the inner density (Del Popolo 2009, Del Popolo 2012; El-Zant et al. 2001, El-Zant et al. 2004; Romano-Díaz et al. 2008, Romano-Díaz et al. 2009).

As already reported, NFW N-body simulations predicted a profile with inner slope $\propto r^{-1}$ and an outer one $\propto r^{-3}$. More recently, it has been shown that the density profiles are better fitted by an Einasto profile which becomes shallower towards the centre of the halo (e.g. Navarro et al. 2010). In any case, the lower values for the inner slope obtained in N-body simulations are $\alpha = 0.8$ at 120 pc (Stadel et al. 2009) in agreement to analytical and numerical works to solve the Jeans equation (Austin et al. 2005; Dehnen & McLaughlin 2005). Inner density slopes in the range $0.7 < \alpha < 1.5$ could be considered in agreement with Λ CDM predictions (SA07).

However, as reported in the introduction, slopes flatter than those obtained in the simulations, $\alpha < 0.7$ are observed in some clusters (Sand et al. 2002, Sand et al. 2004, Sand et al. 2008; Newman et al. 2009, Newman et al. 2011) and the largest numbers of dwarf galaxies and LSBs, and, as previously reported, also some of our clusters have slopes $\alpha < 0.7$.

This discrepancy does not necessarily imply a problem for the Λ CDM model (e.g. see DP09; Governato et al. 2010).

Given the several and noteworthy pieces of evidence supporting Λ CDM on large scales, the discrepancy could be connected to the fact that baryonic physics is a fundamental issue in cluster formation. It could originate just because we are comparing dissipationless systems generated by N-body simulations with real, dissipational structures, whose physics is different from the dissipationless physics typical of DM. We should not forget that the inner 10 kpc of clusters are dominated by baryons (e.g., Sand et al. 2002, Sand et al. 2004, Sand et al. 2008; Newman et al. 2009, Newman et al. 2011) whose presence strongly influence the DM distribution. While baryons can steepen the inner slope of the density profile of clusters through the adiabatic contraction of DM (Blumenthal et al. 1986; Gnedin et al. 2004; Gustafsson et al. 2006), heating of DM due to dynamical friction with cluster galaxies can counteract the adiabatic contraction effect and flatten the inner profile (El-Zant et al. 2001, El-Zant et al. 2004; Romano-Díaz et al. 2008).

Table 3. Results on dark matter profiles for the clusters, from the fits that includes DM, X-ray emitting gas, and BCG. The first column includes names of galaxy cluster, while the second, third and sixth column refers to the NFW fit: second shows the r_s parameter from NFW model for dark matter, third shows the concentration parameter $c_{200} = R_{200}/R_s$, sixth the $\chi^2/\text{d.o.f.}$ goodness of fit. In the case of the gNFW, we give the inner value of α , in seventh column, while in eighth column is reported the $\chi^2/\text{d.o.f.}$ goodness of fit. Fourth column shows the mass of baryonic matter in clusters, and fifth shows the fraction of baryonic matter. Confidence limits are 68 per cent.

Name	Dark matter profiles						
	r_s Mpc	NFW profile ($\alpha=1$)		$f_{M_b/M_{tot}}$	$\chi^2/\text{d.o.f.}$	NFW (α is free parameter)	
		c_{200}	M_b $10^{13} M_\odot$			α	$\chi^2/\text{d.o.f.}$
A85	0.69 ^{+0.13} _{-0.20}	3.15 ^{+0.23} _{-0.32}	42.86 ^{+4.83} _{-6.46}	0.166	1.11	0.85 ^{+0.16} _{-0.28}	2.11
A119	0.54 ^{+0.13} _{-0.12}	3.83 ^{+0.35} _{-0.33}	47.97 ^{+8.35} _{-9.12}	0.199	2.46	0.82 ^{+0.27} _{-0.25}	2.57
A133	0.24 ^{+0.13} _{-0.06}	7.83 ^{+0.35} _{-0.46}	35.02 ^{+3.87} _{-6.45}	0.214	1.55	0.69 ^{+0.08} _{-0.08}	1.22
A168	0.18 ^{+0.07} _{-0.06}	7.03 ^{+0.17} _{-0.20}	19.76 ^{+2.17} _{-3.17}	0.293	1.37	1.01 ^{+0.17} _{-0.11}	2.04
A209	0.58 ^{+0.08} _{-0.11}	2.86 ^{+0.27} _{-0.37}	10.47 ^{+1.85} _{-1.82}	0.087	2.01	1.72 ^{+0.16} _{-0.13}	1.53
A262	0.11 ^{+0.03} _{-0.02}	9.75 ^{+1.11} _{-0.93}	7.25 ^{+1.53} _{-1.67}	0.246	1.64	0.69 ^{+0.03} _{-0.04}	1.39
A383	0.43 ^{+0.13} _{-0.16}	3.32 ^{+0.27} _{-0.32}	11.03 ^{+3.11} _{-2.18}	0.195	1.55	1.58 ^{+0.22} _{-0.22}	1.02
A399	1.22 ^{+0.38} _{-0.46}	2.01 ^{+0.47} _{-0.43}	94.53 ^{+10.11} _{-9.16}	0.249	1.89	0.51 ^{+0.17} _{-0.15}	2.47
A401	0.84 ^{+0.26} _{-0.27}	3.00 ^{+0.28} _{-0.23}	75.91 ^{+6.31} _{-5.83}	0.199	2.05	0.86 ^{+0.29} _{-0.37}	2.13
A478	0.51 ^{+0.16} _{-0.11}	4.04 ^{+0.41} _{-0.58}	30.86 ^{+2.88} _{-3.17}	0.132	1.44	0.96 ^{+0.22} _{-0.16}	1.24
A496	0.13 ^{+0.06} _{-0.06}	10.73 ^{+1.83} _{-1.81}	10.86 ^{+1.51} _{-1.22}	0.119	2.46	0.82 ^{+0.05} _{-0.07}	1.42
A521	0.11 ^{+0.05} _{-0.05}	10.77 ^{+1.43} _{-1.28}	14.47 ^{+1.95} _{-2.17}	0.200	1.42	0.93 ^{+0.12} _{-0.13}	1.19
A539	0.15 ^{+0.04} _{-0.05}	10.21 ^{+1.44} _{-1.21}	15.06 ^{+1.25} _{-1.19}	0.179	1.79	1.08 ^{+0.21} _{-0.22}	2.32
A576	0.51 ^{+0.13} _{-0.12}	4.03 ^{+0.33} _{-0.21}	23.87 ^{+2.14} _{-2.11}	0.113	1.11	0.74 ^{+0.18} _{-0.18}	1.63
A644	1.12 ^{+0.33} _{-0.19}	2.00 ^{+0.22} _{-0.21}	44.62 ^{+3.17} _{-2.91}	0.137	1.37	1.03 ^{+0.11} _{-0.06}	1.55
A697	0.20 ^{+0.10} _{-0.05}	5.21 ^{+0.61} _{-0.52}	13.49 ^{+1.17} _{-1.19}	0.099	0.99	0.94 ^{+0.14} _{-0.13}	4.32
A754	2.84 ^{+0.29} _{-0.38}	0.84 ^{+0.32} _{-0.12}	61.80 ^{+6.17} _{-5.19}	0.153	1.53	1.08 ^{+0.12} _{-0.09}	1.98
A773	0.55 ^{+0.09} _{-0.10}	3.04 ^{+0.41} _{-0.33}	24.47 ^{+2.15} _{-1.98}	0.173	1.73	0.82 ^{+0.13} _{-0.11}	4.22
A780	0.15 ^{+0.05} _{-0.03}	9.05 ^{+0.81} _{-0.73}	40.35 ^{+3.71} _{-3.78}	0.228	2.28	0.92 ^{+0.04} _{-0.07}	0.77
A907	0.22 ^{+0.04} _{-0.05}	6.01 ^{+1.11} _{-0.80}	13.12 ^{+1.13} _{-1.19}	0.200	2.00	1.12 ^{+0.13} _{-0.12}	1.18
A963	0.35 ^{+0.10} _{-0.11}	4.13 ^{+0.51} _{-0.69}	22.63 ^{+2.14} _{-2.18}	0.275	2.75	1.52 ^{+0.13} _{-0.12}	1.83
A1060	0.15 ^{+0.05} _{-0.02}	9.58 ^{+1.45} _{-1.17}	24.28 ^{+2.13} _{-1.93}	0.247	2.47	0.89 ^{+0.08} _{-0.11}	3.16
A1068	0.53 ^{+0.11} _{-0.13}	2.75 ^{+0.51} _{-0.32}	14.64 ^{+1.16} _{-1.19}	0.189	1.89	0.98 ^{+0.19} _{-0.19}	1.54
A1201	0.20 ^{+0.10} _{-0.06}	5.88 ^{+0.63} _{-0.61}	9.79 ^{+1.15} _{-0.93}	0.180	1.80	1.72 ^{+0.10} _{-0.10}	2.22
A1240	0.21 ^{+0.08} _{-0.10}	6.11 ^{+0.18} _{-0.25}	16.42 ^{+1.73} _{-1.67}	0.223	2.23	0.91 ^{+0.08} _{-0.08}	2.21
A1361	0.22 ^{+0.06} _{-0.06}	6.81 ^{+0.63} _{-0.51}	21.56 ^{+2.15} _{-2.17}	0.194	1.94	0.80 ^{+0.29} _{-0.28}	1.50
A1413	0.24 ^{+0.11} _{-0.11}	5.85 ^{+0.42} _{-0.44}	14.48 ^{+1.42} _{-1.18}	0.169	1.69	0.93 ^{+0.08} _{-0.08}	1.99
A1446	0.21 ^{+0.05} _{-0.03}	9.06 ^{+0.67} _{-0.72}	28.20 ^{+2.16} _{-2.17}	0.222	2.22	1.34 ^{+0.73} _{-0.72}	2.37
A1569	0.19 ^{+0.05} _{-0.04}	10.37 ^{+2.01} _{-2.04}	37.01 ^{+3.26} _{-3.17}	0.257	2.57	0.67 ^{+0.18} _{-0.19}	2.12
A1644	0.12 ^{+0.04} _{-0.08}	14.65 ^{+3.89} _{-4.17}	33.95 ^{+4.12} _{-3.16}	0.232	2.32	0.75 ^{+0.07} _{-0.07}	3.11
A1650	1.44 ^{+0.33} _{-0.29}	1.83 ^{+0.35} _{-0.37}	81.43 ^{+5.85} _{-4.81}	0.206	2.06	0.43 ^{+0.12} _{-0.22}	2.22
A1651	0.51 ^{+0.16} _{-0.17}	3.69 ^{+0.74} _{-0.71}	37.81 ^{+3.75} _{-3.61}	0.194	1.94	0.91 ^{+0.22} _{-0.08}	2.18
A1664	0.29 ^{+0.11} _{-0.14}	6.64 ^{+0.83} _{-0.81}	40.35 ^{+3.71} _{-3.78}	0.176	1.76	0.72 ^{+0.26} _{-0.25}	2.36
A1689	0.21 ^{+0.05} _{-0.05}	7.15 ^{+0.91} _{-0.85}	39.52 ^{+4.17} _{-3.92}	0.245	2.45	1.10 ^{+0.18} _{-0.16}	1.54
A1736	0.10 ^{+0.00} _{-0.01}	15.87 ^{+4.16} _{-4.13}	11.26 ^{+1.93} _{-2.18}	0.138	1.38	1.08 ^{+0.13} _{-0.27}	2.34
A1795	0.43 ^{+0.20} _{-0.21}	4.21 ^{+0.55} _{-0.88}	20.46 ^{+3.16} _{-2.19}	0.105	1.05	1.04 ^{+0.45} _{-0.28}	2.13
A1835	0.87 ^{+0.18} _{-0.27}	2.36 ^{+0.35} _{-0.44}	41.93 ^{+5.16} _{-4.28}	0.183	1.83	0.68 ^{+0.13} _{-0.15}	1.77
A1914	3.05 ^{+0.48} _{-0.37}	0.74 ^{+0.36} _{-0.33}	93.76 ^{+9.61} _{-10.27}	0.121	1.21	0.43 ^{+0.18} _{-0.18}	1.28
A1995	0.88 ^{+0.33} _{-0.28}	2.77 ^{+0.38} _{-0.33}	56.22 ^{+6.17} _{-4.91}	0.124	1.24	0.55 ^{+0.18} _{-0.18}	1.22
A2029	0.37 ^{+0.17} _{-0.19}	6.39 ^{+0.41} _{-0.43}	42.42 ^{+5.18} _{-4.19}	0.126	1.26	0.91 ^{+0.37} _{-0.17}	2.20
A2034	0.90 ^{+0.23} _{-0.22}	2.37 ^{+0.49} _{-0.42}	21.22 ^{+1.93} _{-2.18}	0.106	1.06	1.06 ^{+0.37} _{-0.27}	2.38
A2052	0.13 ^{+0.03} _{-0.04}	9.63 ^{+1.13} _{-1.13}	13.45 ^{+1.28} _{-1.28}	0.147	1.47	1.62 ^{+0.27} _{-0.22}	2.32
A2063	0.22 ^{+0.11} _{-0.05}	6.89 ^{+0.48} _{-0.43}	20.06 ^{+2.47} _{-2.46}	0.194	1.94	0.80 ^{+0.27} _{-0.28}	0.92
A2065	1.22 ^{+0.21} _{-0.18}	2.02 ^{+0.34} _{-0.46}	94.05 ^{+10.27} _{-11.28}	0.238	2.38	0.41 ^{+0.29} _{-0.27}	1.30
A2124	0.11 ^{+0.04} _{-0.02}	10.76 ^{+1.84} _{-1.81}	20.67 ^{+2.15} _{-2.19}	0.157	1.57	0.91 ^{+0.12} _{-0.16}	2.47
A2142	0.50 ^{+0.12} _{-0.11}	5.10 ^{+0.43} _{-0.49}	21.69 ^{+3.16} _{-1.28}	0.072	0.72	0.93 ^{+0.12} _{-0.17}	1.29
A2147	0.16 ^{+0.02} _{-0.03}	10.06 ^{+1.81} _{-1.27}	18.09 ^{+2.52} _{-1.27}	0.165	1.65	1.12 ^{+0.19} _{-0.19}	2.28
A2163	2.00 ^{+0.47} _{-0.45}	1.88 ^{+0.27} _{-0.23}	143.51 ^{+14.92} _{-15.37}	0.129	1.29	0.51 ^{+0.14} _{-0.15}	0.75
A2199	0.24 ^{+0.09} _{-0.10}	5.98 ^{+0.45} _{-0.36}	24.25 ^{+2.38} _{-2.19}	0.195	1.95	0.90 ^{+0.39} _{-0.10}	2.17
A2204	0.76 ^{+0.21} _{-0.17}	2.56 ^{+0.42} _{-0.54}	43.67 ^{+5.82} _{-5.19}	0.186	1.86	0.85 ^{+0.36} _{-0.37}	2.28
A2218	0.21 ^{+0.05} _{-0.03}	6.13 ^{+1.14} _{-0.65}	8.95 ^{+2.15} _{-0.93}	0.138	1.38	1.78 ^{+0.14} _{-0.15}	2.10
A2219	0.66 ^{+0.15} _{-0.17}	3.24 ^{+0.43} _{-0.53}	47.06 ^{+5.38} _{-4.19}	0.128	1.28	0.83 ^{+0.37} _{-0.33}	1.18
A2244	1.12 ^{+0.25} _{-0.27}	2.23 ^{+0.34} _{-0.31}	35.20 ^{+4.16} _{-3.82}	0.096	0.96	0.81 ^{+0.16} _{-0.17}	2.19
A2256	2.67 ^{+0.44} _{-0.17}	1.06 ^{+0.47} _{-0.37}	57.77 ^{+5.97} _{-6.92}	0.120	1.20	1.12 ^{+0.11} _{-0.27}	1.11

Table 3. Continued.

Name	Dark matter profiles				$f_{M_b/M_{tot}}$	$\chi^2/\text{d.o.f.}$	NFW (α is free parameter)	
	r_s Mpc	NFW profile ($\alpha=1$)		α			$\chi^2/\text{d.o.f.}$	
		c_{200}	M_b $10^{13} M_\odot$					
RXCJ2337.6+0016	$0.29^{+0.06}_{-0.03}$	$4.72^{+0.55}_{-0.77}$	$13.75^{+1.44}_{-1.55}$	0.131	1.61	$1.67^{+0.19}_{-0.19}$	1.18	
ZwCL1215	$0.41^{+0.08}_{-0.16}$	$5.12^{+0.42}_{-0.51}$	$36.33^{+3.17}_{-2.38}$	0.118	1.08	$0.74^{+0.14}_{-0.13}$	1.14	
RCSJ0224-0002	$0.51^{+0.09}_{-0.17}$	$2.48^{+0.35}_{-0.35}$	$22.45^{+0.19}_{-0.11}$	0.113	2.13	$1.02^{+0.15}_{-0.14}$	1.39	
RCSJ0439-2904	$0.20^{+0.01}_{-0.03}$	$3.92^{+0.35}_{-0.23}$	$9.01^{+1.66}_{-1.47}$	0.207	2.37	$1.84^{+0.36}_{-0.33}$	2.20	
RCSJ1107-0523	$0.34^{+0.03}_{-0.03}$	$2.75^{+0.36}_{-0.35}$	$12.65^{+1.47}_{-1.48}$	0.219	2.39	$1.53^{+0.54}_{-0.53}$	1.25	
RCSJ1419.2+5326	$0.22^{+0.03}_{-0.05}$	$5.74^{+0.53}_{-0.31}$	$33.91^{+2.88}_{-3.17}$	0.222	2.62	$0.67^{+0.12}_{-0.13}$	1.28	
RCSJ1620+2929	$0.31^{+0.15}_{-0.06}$	$3.68^{+0.42}_{-0.41}$	$14.15^{+1.47}_{-1.82}$	0.147	1.87	$1.04^{+0.14}_{-0.15}$	1.17	
RCS2156+0123	$1.77^{+0.22}_{-0.34}$	$1.03^{+0.43}_{-0.33}$	$42.97^{+5.82}_{-5.28}$	0.181	1.88	$0.58^{+0.11}_{-0.12}$	1.25	
RCSJ2318+0034	$1.65^{+0.23}_{-0.25}$	$1.08^{+0.29}_{-0.27}$	$51.45^{+5.27}_{-5.82}$	0.141	1.81	$0.64^{+0.15}_{-0.14}$	1.10	
RCSJ2319+0038	$0.57^{+0.11}_{-0.09}$	$2.92^{+0.36}_{-0.35}$	$91.91^{+8.88}_{-9.45}$	0.204	2.24	$0.54^{+0.15}_{-0.16}$	2.36	
RXJ0439.0+0520	$0.17^{+0.05}_{-0.03}$	$7.31^{+0.27}_{-0.77}$	$11.43^{+2.16}_{-1.37}$	0.225	1.25	$1.04^{+0.29}_{-0.38}$	2.46	
RXJ0848.7+4456	$1.33^{+0.34}_{-0.27}$	$0.57^{+0.15}_{-0.11}$	$9.36^{+3.56}_{-2.19}$	0.241	2.81	$1.01^{+0.14}_{-0.12}$	1.66	
RXJ0849+4452	$1.73^{+0.37}_{-0.25}$	$0.74^{+0.21}_{-0.12}$	$67.87^{+6.48}_{-6.84}$	0.165	1.45	$0.55^{+0.17}_{-0.16}$	1.28	
RXJ0910+5422	$0.83^{+0.15}_{-0.19}$	$2.44^{+0.15}_{-0.11}$	$66.84^{+6.77}_{-7.55}$	0.143	1.03	$0.63^{+0.13}_{-0.13}$	2.46	
RXJ1113.1-2615	$0.26^{+0.06}_{-0.04}$	$2.98^{+0.23}_{-0.21}$	$12.72^{+1.49}_{-1.48}$	0.219	2.39	$1.04^{+0.33}_{-0.37}$	2.22	
RXJ1221.4+4918	$1.01^{+0.15}_{-0.11}$	$2.02^{+0.27}_{-0.25}$	$75.08^{+6.32}_{-4.29}$	0.151	1.61	$0.54^{+0.18}_{-0.18}$	1.27	

5 DISCUSSION

As discussed in the paper, our analysis used Chandra data and similar methods to that of SA07, but our sample is larger. Confronting our tables and those of SA07, we see several clusters common to the two studies (e.g., A1795; A2029; A478; A1413; A2204; A383; A963; A1835; A611; A2537; MACSJ0242.6-2132; MACSJ1427.6-2521; MACSJ2229.8-2756; MACSJ1391.8-2635; MACSJ1115.8+0129; MACSJ1720.3+3536; MACSJ1311.0-0311; MACSJ1423.8+2404). The inner slopes of these clusters are compatible in our and SA07 study.

Other clusters, like A383, A611, A963, A1835, A2029, A2204, A2589 were studied by others authors. For example, A611 was studied by Newman et al. (2009) who combined weak lensing from multicolor Subaru imaging, strong lensing (Hubble Space Telescope) and stellar velocity dispersion measures (Keck Telescope), sampling the dark matter profile from 3 kpc to 3.25 Mpc. Newman et al. (2009) found values of $r_s = 320^{+240}_{-110}$ kpc and $c = 5.1^{+1.7}_{-1.6}$ (in agreement with SA07), but $\alpha < 0.3$ (< 0.56 , < 0.65) at 68 per cent (95 per cent, 99 per cent) CL. SA07 found a value of the slope $\alpha = 0.64^{+0.94}$. A383 was studied by S08 finding a flat inner DM slope ($\alpha = 0.45^{+0.2}_{-0.25}$), and by Newman et al. (2011) who found $\alpha < 1$ at (95 per cent confidence) and a best fit (inferred from weak and strong lensing, kinematics and X-ray data) of $\alpha = 0.59^{+0.30}_{-0.35}$. SA07 found $\alpha < 0.8$, we found $\alpha = 1.58^{+0.22}_{-0.22}$.

A flat slope was obtained also for A963 by Sand et al. (2008), but Bartelmann & Meneghetti (2004), Dalal & Keeton (2003) and SA07 found values consistent with the NFW model. We found $\alpha = 1.52^{0.13}_{-0.12}$. In the case of A2029, Lewis et al. (2003) found $\alpha = 1.19 \pm 0.04$ similarly to SA07, and we got $0.91^{+0.37}_{-0.17}$. In the case of A1835, A2029, A2204, Arabadjis et al. (2004) by means of Chandra data

obtained $\alpha \simeq 0.9$, $\alpha \simeq 1.85$, and $\alpha \simeq 1.8$, respectively, much larger than SA07 values and ours.

As reported, Newman et al. (2009), Newman et al. (2011), presented a detailed analysis of DM and baryonic distributions in A611, and A383 combining weak lensing, strong lensing and stellar velocity dispersion for the BCG, and finding slopes flatter than the NFW predictions. According to Newman et al. (2009), Newman et al. (2011), degeneracies in constraining the DM profile can be broken only simultaneously using the three techniques. In reality, the X-ray observations alone give information on clusters on cluster structure in the range 500-50 kpc. At smaller radii, temperature determination is limited by instrumental resolution, substructure (SA07), and they are also limited by “cooling flows” presence and the breaking of assumption of hydrostatic equilibrium (see Arabadjis et al. 2004).

So, if the Newman et al. (2009) and Newman et al. (2011) point of view is correct, for clusters containing larger quantity of baryons the inner profile may be flatter than X-ray observations. SA07 tried to understand how important was the role of central BCG in MS2137.3-2353 (for which Sand et al. (2002), Sand et al. (2004) found a flat profile). Varying the ratio M/L_V they observed, in agreement with Newman et al. (2009) and Newman et al. (2011) a flattening of the profile, but in any case the slope was still compatible with a NFW fit (differently from Newman et al. (2009), Newman et al. (2011)).

Other systematic uncertainties that could change the results is the presence of non-thermal pressure support (due to gas motions, cosmic rays or magnetic fields), however for relaxed clusters, bulk and/or turbulent motions, if present, could cause changes in the mass measurements of 10-20 per cent accuracy (Nagai et al. 2007; Rasia et al. 2006). Similar effects are expected by magnetic pressure Dolag & Schindler (2000).

Another important issue to recall is the fact that in

the present paper, as in that of SA07 the X-ray data only extend to about r_{2500} (approximately a quarter to a third of the virial radius in most clusters), so, for example, the claim that the mass-concentration relation is appropriate for the virial radii, is not totally true.

6 CONCLUSIONS

We presented the reconstruction of the total mass (dark matter, gas and luminous matter) from the Chandra observations of 129 massive X-ray luminous galaxy clusters in the redshift range 0.01 – 1.4. We estimated the total (M_{tot}) mass within R_{200} in the range $3 - 293 \times 10^{14} M_{\odot}$.

In order to estimate the fraction of dark matter and gas we have used the conditions of hydrostatic equilibrium and spherical symmetry. Similarly to SA07, we performed two different analysis: the first concerning the total mass of the clusters, and the second decomposing the total mass in its diffuse gas, DM, and BCG components.

Similarly to SA07, the NFW gives a good fit to the total mass and DM distribution. We obtained a best-fitting result for the inner slope of the DM profile in the clusters $\alpha = 0.94 \pm 0.13$. We also obtained a mass-concentration relation $c \propto M^a / (1+z)^b$, with $a = -0.56 \pm 0.15$ and $b = 0.80 \pm 0.25$ (68 per cent confidence limits) in agreement with previous results and simulations.

Finally, we showed that there is a tight correlation among the inner slope α and the baryonic mass, M_b , content.

ACKNOWLEDGMENTS

This research has made use of data obtained from the Chandra Data Archive and the Chandra Source Catalog, and software provided by the Chandra X-ray Center (CXC) in the application packages CIAO, ChIPS, and Sherpa. We thank all the staff members involved in the Chandra project. Iu. Babyk and I. Vavilova note that this work was partially supported in frame of the "CosmoMicroPhysics" Program and Target Project of the Physics and Astronomy Division of the NAS of Ukraine.

REFERENCES

Abadi M. G., Navarro J. F., Fardal M., Babul A., Steinmetz M., 2010, MNRAS , 407, 435
 Allen S. W., Schmidt R. W., Fabian A. C., 2002, MNRAS , 335, 256
 Arabadjis J. S., Bautz M. W., Arabadjis G., 2004, ApJ , 617, 303
 Arabadjis J. S., Bautz M. W., Garmire G. P., 2002, ApJ , 572, 66
 Ascasibar Y., Hoffman Y., Gottlöber S., 2007, MNRAS , 376, 393
 Ascasibar Y., Yepes G., Gottlöber S., Müller V., 2004, MNRAS , 352, 1109
 Austin C. G., Williams L. L. R., Barnes E. I., Babul A., Dalcanton J. J., 2005, ApJ , 634, 756
 Babyk I., Elyiv A., Melnyk O., Krivodubskij V. N., 2012, Kinematics and Physics of Celestial Bodies, 28, 69

Babyk I., Melnyk O., Elyiv A., 2012, Advances in Astronomy and Space Physics, 2, 56
 Babyk I., Vavilova I. B., 2012, in Micaelian A. M., Malkov O. Y., Samus N. N., eds, Fifty years of Cosmic Era: Real and Virtual Studies of the Sky. Conference of Young Scientists of CIS Countries The dark matter distribution in the Abell 1689 galaxy cluster. pp 162–167
 Babyk I. V., 2012, Bulletin Crimean Astrophysical Observatory, 108, 87
 Bartelmann M., Meneghetti M., 2004, A&A, 418, 413
 Bertschinger E., 1985, ApJS, 58, 39
 Blumenthal G. R., Faber S. M., Flores R., Primack J. R., 1986, ApJ , 301, 27
 Bradač M., Erben T., Schneider P., Hildebrandt H., Lombardi M., Schirmer M., Miralles J.-M., Clowe D., Schindler S., 2005, A&A, 437, 49
 Bradač M., Schrabback T., Erben T., McCourt M., Million E., Mantz A., Allen S., Blandford R., Halkola A., Hildebrandt H., Lombardi M., Marshall P., Schneider P., Treu T., Kneib J.-P., 2008, ApJ , 681, 187
 Brough S., Couch W. J., Collins C. A., Jarrett T., Burke D. J., Mann R. G., 2008, MNRAS , 385, L103
 Bullock J. S., Dekel A., Kolatt T. S., Kravtsov A. V., Klypin A. A., Porciani C., Primack J. R., 2001, ApJ , 555, 240
 Cen R., Dong F., Bode P., Ostriker J. P., 2004, ArXiv Astrophysics e-prints
 Dalal N., Keeton C. R., 2003, ArXiv Astrophysics e-prints
 de Blok W. J. G., Bosma A., 2002, A&A, 385, 816
 de Blok W. J. G., Bosma A., McGaugh S., 2003, MNRAS , 340, 657
 de Blok W. J. G., Walter F., Brinks E., Trachternach C., Oh S.-H., Kennicutt Jr. R. C., 2008, AJ, 136, 2648
 Debattista V. P., Moore B., Quinn T., Kazantzidis S., Maas R., Mayer L., Read J., Stadel J., 2008, ApJ , 681, 1076
 Dehnen W., McLaughlin D. E., 2005, MNRAS , 363, 1057
 Del Popolo A., 2009, ApJ , 698, 2093
 Del Popolo A., 2012, MNRAS , 419, 971
 Del Popolo A., Gambera M., Recami E., Spedicato E., 2000, A&A, 353, 427
 Dickey J. M., Lockman F. J., 1990, ARA&A, 28, 215
 Dolag K., Bartelmann M., Perrotta F., Baccigalupi C., Moscardini L., Meneghetti M., Tormen G., 2004, A&A, 416, 853
 Dolag K., Schindler S., 2000, A&A, 364, 491
 Edge A. C., Stewart G. C., 1991, MNRAS , 252, 428
 Eke V. R., Navarro J. F., Steinmetz M., 2001, ApJ , 554, 114
 El-Zant A., Shlosman I., Hoffman Y., 2001, ApJ , 560, 636
 El-Zant A. A., Hoffman Y., Primack J., Combes F., Shlosman I., 2004, ApJ , 607, L75
 Ettori S., Fabian A. C., Allen S. W., Johnstone R. M., 2002, MNRAS , 331, 635
 Fillmore J. A., Goldreich P., 1984, ApJ , 281, 1
 Flores R. A., Primack J. R., 1994, ApJ , 427, L1
 Gao L., White S. D. M., 2007, MNRAS , 377, L5
 Gavazzi R., 2005, A&A, 443, 793
 Gavazzi R., Fort B., Mellier Y., Pelló R., Dantel-Fort M., 2003, A&A, 403, 11
 Gentile G., Salucci P., Klein U., Vergani D., Kalberla P., 2004, MNRAS , 351, 903

- Gnedin O. Y., Kravtsov A. V., Klypin A. A., Nagai D., 2004, *ApJ* , 616, 16
- Governato F., Brook C., Mayer L., Brooks A., Rhee G., Wadsley J., Jonsson P., Willman B., Stinson G., Quinn T., Madau P., 2010, *Nature* , 463, 203
- Gunn J. E., 1977, *ApJ* , 218, 592
- Gunn J. E., Gott III J. R., 1972, *ApJ* , 176, 1
- Gustafsson M., Fairbairn M., Sommer-Larsen J., 2006, *Phys. Rev. D* , 74, 123522
- Haarsma D. B., Leisman L., Donahue M., Bruch S., Böhringer H., Croston J. H., Pratt G. W., Voit G. M., Arnaud M., Pierini D., 2010, *ApJ* , 713, 1037
- Hayashi E., Navarro J. F., Power C., Jenkins A., Frenk C. S., White S. D. M., Springel V., Stadel J., Quinn T. R., 2004, *MNRAS* , 355, 794
- Hiotelis N., 2002, *A&A*, 382, 84
- Hoffman Y., Shaham J., 1985, *ApJ* , 297, 16
- Hudson M. J., Ebeling H., 1997, *ApJ* , 479, 621
- Humphrey P. J., Buote D. A., Gastaldello F., Zappacosta L., Bullock J. S., Brighenti F., Mathews W. G., 2006, *ApJ* , 646, 899
- Jaffe W., 1983, *MNRAS* , 202, 995
- Jing Y. P., Suto Y., 2000, *ApJ* , 529, L69
- Klypin A., Kravtsov A. V., Bullock J. S., Primack J. R., 2001, *ApJ* , 554, 903
- Kneib J.-P., Hudelot P., Ellis R. S., Treu T., Smith G. P., Marshall P., Czoske O., Smail I., Natarajan P., 2003, *ApJ* , 598, 804
- Kuzio de Naray R., McGaugh S. S., de Blok W. J. G., 2008, *ApJ* , 676, 920
- Kuzio de Naray R., McGaugh S. S., Mihos J. C., 2009, *ApJ* , 692, 1321
- Lahav O., Lilje P. B., Primack J. R., Rees M. J., 1991, *MNRAS* , 251, 128
- Le Delliou M., Henriksen R. N., 2003, *A&A*, 408, 27
- Lewis A. D., Buote D. A., Stocke J. T., 2003, *ApJ* , 586, 135
- Limousin M., Richard J., Kneib J.-P., Brink H., Pelló R., Jullo E., Tu H., Sommer-Larsen J., Egami E., Michałowski M. J., Cabanac R., Stark D. P., 2008, *A&A*, 489, 23
- Lin Y.-T., Mohr J. J., 2004, *ApJ* , 617, 879
- Loeb A., Peebles P. J. E., 2003, *ApJ* , 589, 29
- Ma C.-P., Chang P., Zhang J., 2009, *ArXiv e-prints*
- Mahdavi A., Hoekstra H., Babul A., Sievers J., Myers S. T., Henry J. P., 2007, *ApJ* , 664, 162
- Mashchenko S., Couchman H. M. P., Wadsley J., 2006, *Nature* , 442, 539
- McMillan P. J., Dehnen W., 2005, *MNRAS* , 363, 1205
- Mellier Y., 1999, *ARA&A*, 37, 127
- Milosavljević M., Merritt D., 2001, *ApJ* , 563, 34
- Miralda-Escude J., 1995, *ApJ* , 438, 514
- Moore B., 1994, *Nature* , 370, 629
- Moore B., Governato F., Quinn T., Stadel J., Lake G., 1998, *ApJ* , 499, L5
- Nagai D., Vikhlinin A., Kravtsov A. V., 2007, *ApJ* , 655, 98
- Navarro J. F., Frenk C. S., White S. D. M., 1996, *ApJ* , 462, 563
- Navarro J. F., Frenk C. S., White S. D. M., 1997, *ApJ* , 490, 493
- Navarro J. F., Hayashi E., Power C., Jenkins A. R., Frenk C. S., White S. D. M., Springel V., Stadel J., Quinn T. R., 2004, *MNRAS* , 349, 1039
- Navarro J. F., Ludlow A., Springel V., Wang J., Vogelsberger M., White S. D. M., Jenkins A., Frenk C. S., Helmi A., 2010, *MNRAS* , 402, 21
- Newman A. B., Treu T., Ellis R. S., Sand D. J., 2011, *ApJ* , 728, L39
- Newman A. B., Treu T., Ellis R. S., Sand D. J., Richard J., Marshall P. J., Capak P., Miyazaki S., 2009, *ApJ* , 706, 1078
- O'Sullivan E., Sanderson A. J. R., Ponman T. J., 2007, *MNRAS* , 380, 1409
- Popesso P., Biviano A., Böhringer H., Romaniello M., 2007, *A&A*, 464, 451
- Power C., Navarro J. F., Jenkins A., Frenk C. S., White S. D. M., Springel V., Stadel J., Quinn T., 2003, *MNRAS* , 338, 14
- Rasia E., Ettori S., Moscardini L., Mazzotta P., Borgani S., Dolag K., Tormen G., Cheng L. M., Diaferio A., 2006, *MNRAS* , 369, 2013
- Ricotti M., 2003, *MNRAS* , 344, 1237
- Ricotti M., Pontzen A., Viel M., 2007, *ApJ* , 663, L53
- Ricotti M., Wilkinson M. I., 2004, *MNRAS* , 353, 867
- Romano-Díaz E., Shlosman I., Heller C., Hoffman Y., 2009, *ApJ* , 702, 1250
- Romano-Díaz E., Shlosman I., Hoffman Y., Heller C., 2008, *ApJ* , 685, L105
- Russell H. R., Sanders J. S., Fabian A. C., 2008, *MNRAS* , 390, 1207
- Salucci P., Lapi A., Tonini C., Gentile G., Yegorova I., Klein U., 2007, *MNRAS* , 378, 41
- Sand D. J., Treu T., Ellis R. S., 2002, *ApJ* , 574, L129
- Sand D. J., Treu T., Ellis R. S., Smith G. P., Kneib J.-P., 2008, *ApJ* , 674, 711
- Sand D. J., Treu T., Smith G. P., Ellis R. S., 2004, *ApJ* , 604, 88
- Sanders J. S., Fabian A. C., 2007, *MNRAS* , 381, 1381
- Schmidt R. W., Allen S. W., 2007, *MNRAS* , 379, 209
- Schombert J. M., 1988, *ApJ* , 328, 475
- Shaw L. D., Weller J., Ostriker J. P., Bode P., 2006, *ApJ* , 646, 815
- Simon J. D., Bolatto A. D., Leroy A., Blitz L., Gates E. L., 2005, *ApJ* , 621, 757
- Smith G. P., Kneib J.-P., Ebeling H., Czoske O., Smail I., 2001, *ApJ* , 552, 493
- Smith G. P., Kneib J.-P., Smail I., Mazzotta P., Ebeling H., Czoske O., 2005, *MNRAS* , 359, 417
- Stadel J., Potter D., Moore B., Diemand J., Madau P., Zemp M., Kuhlen M., Quilis V., 2009, *MNRAS* , 398, L21
- Subramanian K., Cen R., Ostriker J. P., 2000, *ApJ* , 538, 528
- Tonini C., Lapi A., Salucci P., 2006, *ApJ* , 649, 591
- Tyson J. A., Kochanski G. P., dell'Antonio I. P., 1998, *ApJ* , 498, L107
- Umetsu K., Broadhurst T., 2008, *ApJ* , 684, 177
- Vikhlinin A., Forman W., Jones C., 1999, *ApJ* , 525, 47
- Weinberg M. D., Katz N., 2002, *ApJ* , 580, 627
- Whiley I. M., Aragón-Salamanca A., De Lucia G., von der Linden A., Bamford S. P., Best P., Bremer M. N., Jablonka P., Johnson O., Milvang-Jensen B., Noll S., Poggianti B. M., Rudnick G., Saglia R., White S., Zaritsky D., 2008, *MNRAS* , 387, 1253
- White S. D. M., Zaritsky D., 1992, *ApJ* , 394, 1

- Williams L. L. R., Babul A., Dalcanton J. J., 2004, ApJ ,
604, 18
Yang X., Mo H. J., van den Bosch F. C., 2008, ApJ , 676,
248
Zappacosta L., Buote D. A., Gastaldello F., Humphrey
P. J., Bullock J., Brighenti F., Mathews W., 2006, ApJ
, 650, 777

This paper has been typeset from a \TeX / \LaTeX file prepared
by the author.